GEOPHYSICS

Destruction and regrowth of lithospheric mantle beneath large igneous provinces

Simon N. Stephenson[1]*, Patrick W. Ball[2], Fred D. Richards[3]

Large igneous provinces (LIPs) are formed by enormous (i.e., frequently >10^6 km^3) but short-lived magmatic events that have profound effects upon global geodynamic, tectonic, and environmental processes. Lithospheric structure is known to modulate mantle melting, yet its evolution during and after such dramatic periods of magmatism is poorly constrained. Using geochemical and seismological observations, we find that magmatism is associated with thin (i.e., ≲80 km) lithosphere and we reveal a striking positive correlation between the thickness of modern-day lithosphere beneath LIPs and time since eruption. Oceanic lithosphere rethickens to 125 km, while continental regions reach >190 km. Our results point to systematic destruction and subsequent regrowth of lithospheric mantle during and after LIP emplacement and recratonization of the continents following eruption. These insights have implications for the stability, age, and composition of ancient, thick, and chemically distinct lithospheric roots, the distribution of economic resources, and emissions of chemical species that force catastrophic environmental change.

INTRODUCTION

The thermomechanical structure of the lithospheric plate and its interaction with the underlying asthenosphere influence the evolution of Earth's topography, plate motions and deformation, the pattern of mantle convection, and the location and style of volcanism (*1–6*). Consequently, lithospheric evolution drives erosional and depositional processes, controls the distribution of economic resources, and influences climatic and environmental conditions through space and time (*7–9*). Geological and geophysical observations provide constraints on present-day lithospheric structure, but only snapshots of its variations through time [e.g., (*8, 10–14*)].

It is often assumed that the lithospheric structure of ancient continental interiors (i.e., cratons) is stable and unchanging over very long time periods, yet there is a paucity of data with which to test this hypothesis [see (*15*) for a comprehensive review]. This interpretation is generally based on the exposure of exclusively ancient, undeformed shields at low elevations with low relief (*16*). These shields overlie a thick, depleted lithospheric mantle (i.e., up to ~250 km in thickness) that is inherently buoyant, viscous, and difficult to convectively remove (*4, 16, 17*). However, several of these cratons are capped by Phanerozoic large igneous provinces (LIPs)—rare, but giant outpourings of lava (>10^6 km^3) that were extruded within geologically short time frames (<5 Ma)—which are commonly linked to the arrival of plume heads beneath the plate (*18*). For example, the Siberian Traps, Central Atlantic Magmatic Province, and Karoo flood basalts overlie the Siberian, West African, and Kalahari cratons, respectively. This association calls into question the assumption that cratonic lithosphere is always thick and stable since a thin tectonic lid is required to generate large volumes of melt, and present-day magmatism is strongly associated with lithosphere <100 km thick (*1, 6, 19–21*).

In this contribution, we attempt to reconcile these seemingly contradictory observations by tracking lithospheric evolution during and after magmatism. We begin by comparing the locations and ages of modern and ancient oceanic islands, seamounts, and plateaux to estimates of plate age and lithospheric thickness. Subsequently, this analysis is extended into continental regions, where we develop conceptual and numerical models to explain the lithospheric response to intraplate magmatic events. Finally, we describe the implications of our results for the thermochemical structure of cratonic lithosphere and their use in addressing several key geodynamic, economic, and environmental questions.

RESULTS

Oceanic intraplate magmatism
Recent intraplate magmatism

Our starting point is to explore lithospheric thickness beneath modern-day intraplate magmatic provinces. In the oceanic realm, the lithospheric mantle cools and thickens away from mid-ocean ridges in a predictable way (*10, 22, 23*). This phenomenon is one of the most widely accepted and well studied in global geophysics. Usefully, it allows expected time-dependent deepening of the lithosphere-asthenosphere boundary (LAB) to be used as a reference template against which deviations in lithospheric thickness can be defined and explored.

We wish to determine whether intraplate magmatism is associated with deviations from the plate-cooling relationship. To carry out this test, we exploit a global database of intraplate magmatic analyses (*20*). This compilation includes major and trace geochemical compositions of mafic rocks at all locations where intraplate magmatism has occurred within the last 10 Ma and has not since moved further than 400 km from the site of eruption (Fig. 1A). We estimate modern-day depth to the LAB, z^1_{LAB}, beneath each recent intraplate magmatic province in three ways. First, z^1_{LAB} beneath each location is extracted from the lithospheric thickness model of Hoggard *et al.* (*8*), which is located by contouring the 1175°C isothermal surface after converting the SL2013sv shear-wave tomographic model into temperature (Fig. 1B). This temperature conversion scheme exploits a calibrated elastic-anelastic

[1]Department of Earth Sciences, University of Oxford, Oxford, UK. [2]Department of Geosciences, Colorado State University, Fort Collins, CO, USA. [3]Department of Earth Science and Engineering, Imperial College London, London, UK.
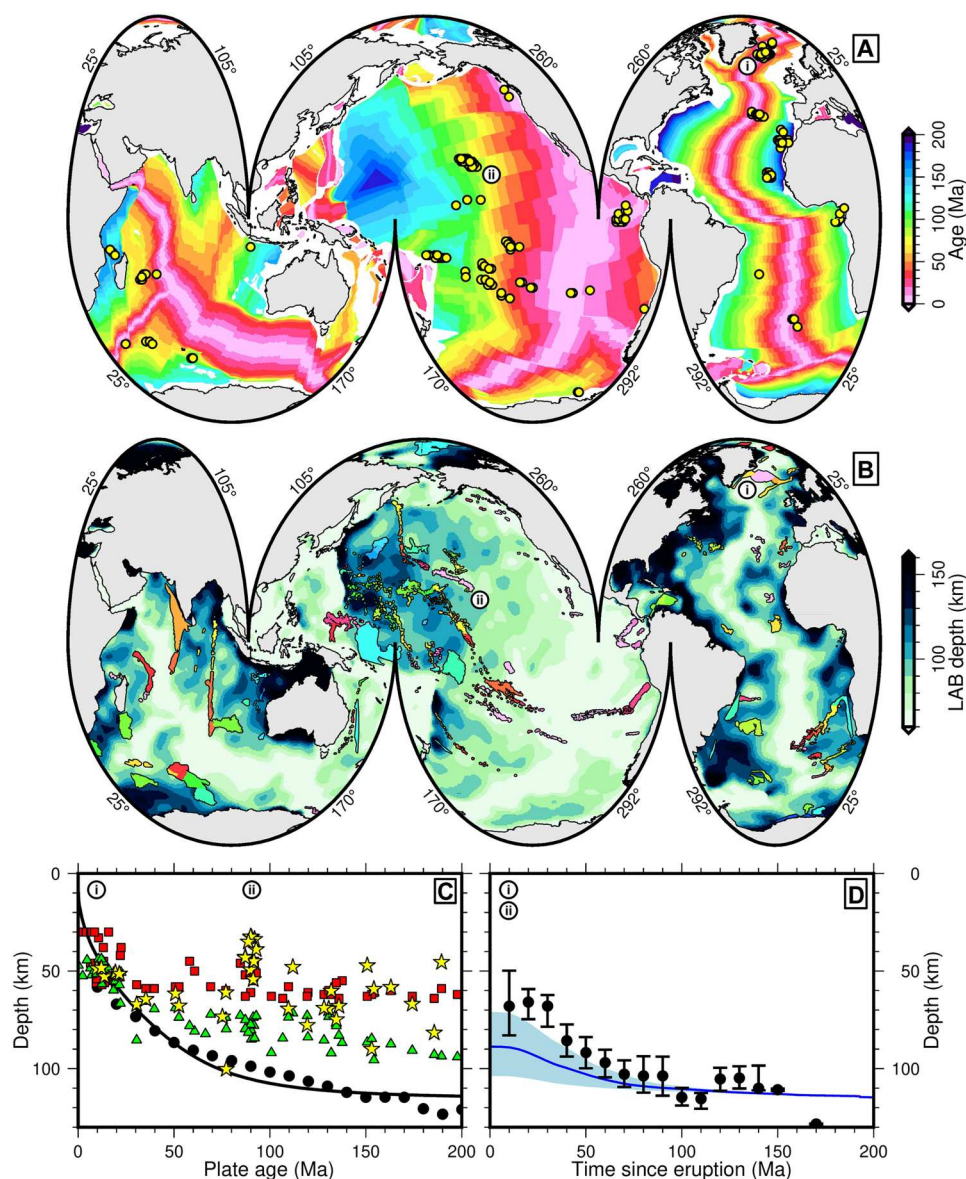*Corresponding author. Email: simon.stephenson@earth.ox.ac.uk

Fig. 1. Distribution of oceanic magmatic provinces. (**A**) Oceanic crustal age (*27, 85*). Yellow circles: locations of intraplate magmatic provinces (*20*). (i) and (ii): locations of Icelandic and Hawaiian hot spots. (**B**) Oceanic LAB depth (*8*). Colored polygons: locations of oceanic magmatic provinces (i.e., ocean islands, seamounts, and plateaux) colored by age. (**C**) Constraints on modern-day LAB depth beneath intraplate magmatic provinces as a function of underlying oceanic crustal age. Red squares: LAB depth determined by inverse modeling of REE compositions of mafic rocks (*20*); green triangles: LAB depth determined by tomographically-derived LAB depth model shown in (B) (*8, 75*); yellow stars: LAB depth estimated by finding magmatic equilibration pressure and temperature that corresponds to base of lithosphere (this study, see main text and Materials and Methods); (i) and (ii): age of crust underlying Icelandic and Hawaiian hot spots. (**D**) Black circles with error bars: modern LAB depth beneath magmatic provinces as a function of province age; moving median at 10-Ma intervals with a ±10 Ma window; error bars: interquartile range; blue line: median expected distribution of LAB depth beneath LIPs if they were distributed randomly in time and space across oceanic lithosphere assuming plate model of Richards *et al.* (*28*) and plate age model of Müller *et al.* (*27*); blue envelope: interquartile range; (i) and (ii): age of Icelandic and Hawaiian hot spots.

parameterization (*24*). Second, we use the lithospheric thickness estimates calculated by inverse modeling of rare earth element (REE) concentrations within mafic intraplate magmas carried out by Ball *et al.* (*20*) (see Materials and Methods). This method is predicated upon the partitioning of REEs between mantle melt and residue during partial melting, where the upper limit of melting is taken to represent the LAB. Finally, we estimate z_{LAB}^1 by calculating melt equilibration pressure, P_{eq}, and temperature, T_{eq}, of intraplate melts

using the thermobarometric scheme developed by Plank and Forsyth (*25*) (dataset S1). This scheme exploits the sensitivity of major oxide phase concentrations within mafic melts to these two properties within the mantle [e.g., (*25, 26*); see Materials and Methods]. The global database of Ball *et al.* (*20*) is filtered for samples where 9 < MgO < 14.5 wt % to mitigate removal or addition of material by fractionation or contamination. Then, T_{eq} and P_{eq} are calculated for the remaining samples. We locate samples that

equilibrated beneath the LAB by selecting samples where $T_{eq} >$ 1175°C. This screening procedure ensures consistency with tomographically determined LAB depths. Next, samples are geographically divided into 1° × 1° bins. We exclude bins with <10 samples since it is unlikely that a very small sample size can be used to accurately locate the base of the lithosphere. Finally, the minimum value of P_{eq} is calculated within each bin, which enables an approximation of maximum depth to the LAB (i.e., $z_{LAB} \approx 31.4\, P_{eq}^{min}$; values of P_{eq} and T_{eq} are given for each sample in the Supplementary Materials).

Figure 1C and fig. S1 show the three independent estimates of observed z_{LAB}^{l} beneath recent oceanic intraplate magmatic provinces (dataset S2). We present our results as a function of the age of oceanic crust, t_{crust}, atop which the magmatic provinces rest (8, 27). All else being equal, z_{LAB}^{l} beneath these recently erupted provinces should be governed entirely by plate cooling as a function of t_{crust}. These observed LAB depth constraints are therefore compared to two estimates of expected, unperturbed LAB depth. First, we calculate expected LAB depth using a plate-cooling model constructed by Richards *et al.* (28) (i.e., black line in Fig. 1C). Second, we compare to the global median LAB depth as a function of oceanic crustal age determined by Hoggard *et al.* (8) (i.e., black circles in Fig. 1C). These two estimates of expected z_{LAB}^{l} values are in close agreement, although it is important to note that they are not entirely independent of one another [see (8, 23, 24)].

For magmatic provinces located above young oceanic crust (i.e., $t_{crust} < 30$ Ma old), predictions and observations are in close agreement, indicating that z_{LAB}^{l} increases from ~20 to 50 km to 60 to 80 km during this time period. For crustal ages $t_{crust} > 30$ Ma, however, expected and observed LAB depths beneath intraplate magmatic provinces dramatically diverge. For an oceanic crustal age, $t_{crust} \gtrsim 30$ Ma old, the plate is systematically thinner by 30 to 60 km than would be expected given the crustal age (compare black line and circles with colored symbols in Fig. 1C). These observations suggest that magmatism occurs exclusively where $z_{LAB} < 100$ km, and in most cases only where $z_{LAB} \lesssim 80$ km.

To make sense of this relationship, consider first the Icelandic hot spot [(i) in Fig. 1]. This magmatic province straddles the Mid-Atlantic Ridge, where lithospheric mantle is thin or absent due to active seafloor spreading. Consequently, all lithospheric thickness proxies suggest that melts are able to ascend to a shallow level, unimpeded by the presence of lithospheric mantle, before encountering the Moho at depths of ~15 to 45 km (29, 30). Next, consider the Hawaiian hot spot, which has $t_{crust} \sim 90$ Ma old [(ii) in Fig. 1]. The LAB ought to be found at $z_{LAB}^{l} \approx 100$ km according to both predicted plate cooling and the global average for oceanic lithosphere of that age. However, major oxide concentrations suggest that Hawaiian melts equilibrate within the asthenosphere to depths as shallow as 30 to 60 km (see yellow stars in Fig. 1C). Furthermore, REE inverse modeling suggests that the top of the asthenospheric melt column is located at 40 to 60 km depth (see red squares in Fig. 1C). Finally, local and global seismic imaging indicates that beneath Hawaii $z_{LAB}^{l} \sim 40$ to 90 km [e.g., (8, 31, 32); see green triangles in Fig. 1C]. This thinner lithosphere is consistent with flexural and gravimetric observations, as well as with xenolith-based thermobarometric results, which indicate that temperatures of 1000° to 1100°C occur at depths of 45 to 55 km beneath Hawaii (33, 34). In contrast to the Icelandic example,

this discrepancy suggests that, locally, z_{LAB}^{l} is notably shallower than expected beneath Hawaii. Together, these considerations strongly suggest that when the plate thickens beyond 70 to 80 km (i.e., when $t_{crust} \gtrsim 30$ Ma old), magmatism is associated with marked lithospheric thinning to depths of 60 to 80 km. In other words, although a precise mechanism cannot be discerned, magmatism is associated with the resetting of z_{LAB} to depths typically found beneath oceanic crust with an age of ~20 to 40 Ma.

Ancient intraplate magmatism
Following cessation of magmatism, lithosphere that is <80 km thick should rethicken as a result of conductive cooling. Modern-day LAB depth, z_{LAB}^{l}, should therefore be thicker beneath older intraplate magmatic provinces than those erupting at present. We test this hypothesis by substantially updating a global map of oceanic plateaux, islands, and seamounts [(35, 36); Fig. 1B, section S2, and dataset S3]. This database contains polygons outlining these oceanic landforms and an associated eruption age (i.e. time elapsed since eruption), t_0, of the magmatic rocks that form them. Polygons are added and excluded, and their age constraints are updated according to recent literature (see section S3 and fig. S2). We sample z_{LAB}^{l} at 0.1° × 0.1° intervals beneath each polygon in our updated database. Once again, we exploit estimates of lithospheric thickness calculated by Hoggard *et al.* (8). Next, we filter our database to ensure that only the final volcanic episode in a given location is included (dataset S4). Thus, we capture the passive response of the lithosphere to magmatism and avoid contamination by subsequent magmatic events. We remove any location that has experienced another phase of magmatism within a distance of <500 km after >30 Ma of the initial eruption. Note, however, that we do not control for any subsequent amagmatic tectonic thinning or thickening of the lithosphere. We calculate the moving median and interquartile range of z_{LAB}^{l} values beneath the remaining intraplate magmatic provinces as a function of t_0. In calculating each median value, we weight the z_{LAB}^{l} value of each point as a function of latitude to avoid biasing moving average estimates toward polar provinces (see Materials and Methods).

On Fig. 1D, the black circles with error bars show observed values of z_{LAB}^{l} as a function of t_0. The median LAB depth beneath the youngest provinces (i.e., where eruption age, $t_0 < 10$ Ma) is consistent with the median thickness calculated for the database of Ball *et al.* (20), as well as our new thermobarometric constraints (see Materials and Methods; section S2.1.1). We find that there is a positive relationship between province age and LAB depth beneath the province up to an age of ~80 to 100 Ma, at which point the deepening of z_{LAB}^{l} flattens off (see black circles with error bars in Fig. 1D). The shape of this relationship resembles a plate cooling model that flattens at a depth consistent with several well-known, published schemes [i.e., 100 to 130 km; Fig. 1 (C and D); e.g., (10, 22, 23)].

Since older oceanic plate is associated with thicker lithosphere, it is possible that any positive relationship between z_{LAB}^{l} and t_0 is generated by chance. This general trend could be produced by distributing intraplate magmatism randomly upon a lithospheric plate whose thickness is governed solely by plate cooling as a function of oceanic crustal age. This relationship would arise because provinces with an eruption age of, say, $t_0 = 180$ Ma can only possibly be found today on old lithosphere, which in the absence of any thermal perturbation would be around 125 km thick [e.g., (23)]. However, recent intraplate magmatism (i.e., $t_0 = 0$ Ma) could theoretically be distributed over lithosphere of thickness ranging from zero at a

mid-ocean ridge to 125 km on the abyssal plain. The median LAB depth of this distribution would therefore be shallower than for those locations overlying only older oceanic crust. As a result, even if z_{LAB}^l is controlled only by oceanic crustal age, younger intraplate magmatism is expected to overlie, on average, thinner lithosphere than sites of older magmatism. A sample of young seamounts, islands, and plateaus would also have a broader distribution of z_{LAB}^l values than older provinces. However, if magmatic emplacement is associated with systematic thinning of the plate (i.e., shallowing of the LAB), then observed values of z_{LAB}^l beneath oceanic plateaus, islands, and seamounts ought to be systematically thinner for any $t_0 < 80$ to 100 Ma than the z_{LAB}^l values expected from plate cooling alone.

To investigate whether temporal trends in z_{LAB}^l provide evidence for magmatism-related lithospheric thinning, we calculate the expected, thermally unperturbed z_{LAB}^l distribution beneath a random sample of oceanic islands, seamounts, and plateaus as a function of t_0 given plate cooling alone (see Materials and Methods). As expected, we find that there is a slight positive relationship between plate age and unperturbed lithospheric thickness beneath ancient oceanic magmatic provinces (see blue line and envelope in Fig. 1D). This predicted distribution is then compared to the observed distribution (i.e., black circles with error bars in

Fig. 1D). Up to an eruption age, $t_0 \approx 90$ Ma before present, ancient magmatic provinces systematically overlie lithosphere that is ~20 to 40 km thinner than would be expected if the plate were not perturbed since seafloor spreading (compare black circles and blue line in Fig. 1D). This result is not materially affected by using alternative lithospheric thickness models (see section S4). This finding further supports our earlier insight that intraplate magmatism resets the plate cooling process by thinning the lithospheric mantle. It is also consistent with seminal work by Detrick and Crough (37), who showed that ocean island subsidence cannot be explained only by seafloor age. Instead, anomalous subsidence requires lithospheric thinning followed by time-dependent rethickening and/or translation away from a subplate thermal anomaly (38). Our results suggest that the thickness of the plate beneath ancient seamounts and plateaus may be better predicted using the eruption age of the province than by oceanic crustal age.

Continental LIPs

The initial rejuvenation and subsequent progressive thickening of the oceanic lithosphere over time following intraplate volcanism raises an important question: Does continental lithosphere behave in a similar way? Answering this question is complicated by the fact that lithospheric thickness in the continental realm—unlike in the oceans—does not generally increase as a function of crustal age.
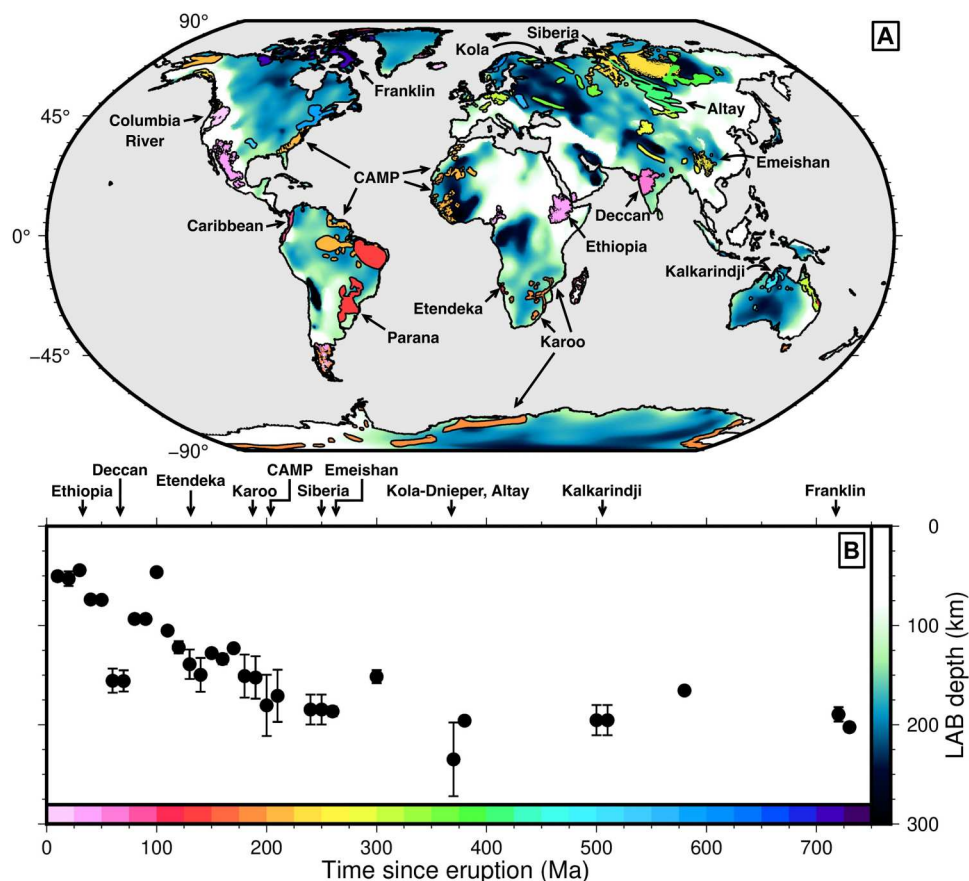

Fig. 2. Global distribution of continental LIPs. (**A**) Distribution of continental LIPs colored by time since their eruption, overlain on map of continental LAB depth (8). Scale bars located on axes of (B); labels indicate names of LIPs mentioned in the main text. (**B**) Modern-day LAB depth beneath LIPs as a function of time since eruption. Labels indicate age of LIPs mentioned in the main text.

Nevertheless, Ball *et al.* (*20*) showed that, by extracting LAB depth from the model of Hoggard *et al.* (*8*) and modeling REE concentrations in intraplate magmas, $z_{LAB}^l \lesssim 100$ km beneath modern continental intraplate magmatic provinces. Similarly, our proxy for z_{LAB}^l based on equilibration pressures and temperatures of major oxide phases in mafic melts agrees that almost all modern magmatic provinces are associated with $z_{LAB}^l \lesssim 80$ km [(*20*); see Materials and Methods; section S2 and fig. S1]. Furthermore, White and McKenzie (*39*) modeled REE concentrations in ancient magmatic provinces. They showed that, irrespective of the often substantial thickness of lithosphere beneath each province today, these ancient mafic magmatic rocks were also associated with thin lithosphere at the time of their formation. The question therefore remains as to how the lithosphere evolves following eruption of intraplate magmatic rocks in the continental realm. We now return to our updated database of ancient intraplate magmatic provinces to explore whether the relationship between z_{LAB} and intraplate magmatism also applies to the continents.

On the continents, this database is mostly composed of LIPs, a dominance that is particularly acute before Cenozoic times. In the same way as our analysis in the oceanic realm, we have expanded and improved the database of Coffin *et al.* (*36*) by refining province ages and polygon outlines using recently published studies (dataset S3). We also now incorporate provinces that are up to 750 Ma old [e.g., (*18*); to access the database and find information on individual changes, see datasets S3 and S4, section S3, and fig. S2]. Similarly, we also again exclude any location where subsequent magmatism occurred within 500 km of the eruption site after 30 Ma of the initial eruption so that only the final phase of intraplate magmatism is included in our database (dataset S4). We again sample z_{LAB}^l within each polygon at 0.1° × 0.1° intervals.

Figure 2 shows depth to the LAB beneath continental LIPs as a function of time since their emplacement [i.e., $z_{LAB}^l(t_0)$]. For the first time, we reveal a striking relationship between LAB depth and time elapsed since continental LIP emplacement. For recent provinces, the lithosphere is ~50 to 70 km thick, which is consistent with that observed in the oceans and a range of geochemical proxies for lithospheric thickness [i.e., estimates calculated by (*20*) and new estimates derived from major element thermobarometry]. LAB depth progressively increases as a function of time since LIP emplacement to approximately 195 km at 250 Ma before flattening off. For example, the Ethiopian Flood Basalts were erupted at t_0 ~ 30 Ma ago, with magmatism continuing to recent times, and are underlain by lithosphere that is <50 km thick (*19*, *20*). The Paraná-Etendeka Traps, where t_0 ~ 138 to 128 Ma ago, on the other hand, are underlain by lithosphere that is 100 to 150 km thick. However, 195-km-thick lithosphere underlies the Siberian Traps, which were erupted at an age of t_0 ~ 250 Ma. This thickness is similar to the LAB depth beneath the ~510-Ma-old Kalkarindji LIP in central and northwestern Australia, and the ~750– to 710-Ma-old Franklin LIP in the Canadian Arctic [e.g., see (*18*); section S2]. The Deccan Traps (age t_0 ~ 66 Ma) mark the only significant outlier to this relationship, having markedly thicker lithosphere than LIPs of a similar age. In general, and with reference to our oceanic analysis, this result hints at lithospheric rejuvenation before, or during, magmatism followed by relaxation after magmatism ceases. Significantly, the depth at which z_{LAB}^l stops increasing

and flattens off (i.e., ~195 km) is about 60 to 90 km deeper than that observed in the oceans (compare Fig. 1D, black circles, and Fig. 2B).

We acknowledge that lateral transport of lava flows or dykes may mean that we sample lithosphere that is far away from the eruption site. In section S4.1, we show the raw, unaveraged values of z_{LAB}^l as a function of eruption age. We further test our results by exploiting two alternative compilations of LIP eruption centers from Torsvik *et al.* (*40*) and a new compilation assembled for this study (see sections S4.2 and S4.3 and dataset S5). We also verify that this relationship is robust against a raft of alternative lithospheric thickness models and is consistent with gravity observations (section S4.2). Finally, it is important to note that our analysis encompasses LIPs erupted onto all types of continental environments, ranging from shields (e.g., eastern Siberian Traps) to Phanerozoic sediments (e.g., Central Atlantic Magmatic Province, i.e., CAMP, and Karoo).

Thermal modeling

It is clear that intraplate magmatism occurs above thinner-than-expected lithosphere and that older magmatic provinces reside above progressively thicker lithosphere. Rifting, which leads to rapid thinning of the lithosphere (i.e., shallowing of the LAB), is usually followed by protracted time-dependent rethickening as a result of conductive cooling. Similarly, the systematic increase in LAB depth beneath magmatic provinces from young to old suggests that the plate thickens as a function of time following the cessation of magmatism. This deepening eventually stalls and flattens out at a constant thickness of around ~195 km beneath continental provinces and ~125 km in the oceans. Two principal models have been developed to explain time-dependent thickening of the lithospheric plate. First, a half-space model, in which the lithosphere cools and thickens indefinitely as a function of age, and second, a plate model, in which the lithosphere cools and thickens, initially closely matching the half-space model, before approaching a finite thickness controlled by the convective resupply of basal heat [e.g., (*10*, *41*)]. The impact of this heating is generally approximated by imposing a constant basal potential temperature, T_p, at a particular depth, z_p, that defines the maximum depth to which conductive cooling can penetrate (*23*, *28*). Note that z_p is not the same as z_{LAB}. Here, we investigate whether conductive cooling, represented in this case by a plate model, can explain the time-dependent thickening of the lithosphere, $z_{LAB}(t)$, following intraplate magmatism.

Oceanic intraplate magmatic provinces

Again, we begin with the oceanic lithosphere. We model one-dimensional thermal evolution, $T(z, t)$, beneath intraplate magmatic provinces and hence depth to the LAB as a function of time, $z_{LAB}(t)$, by making three simple modifications to the plate model of Richards *et al.* (*23*, *28*) (Materials and Methods). First, rather than assuming an initial temperature profile consistent with mid-ocean ridge conditions (i.e., LAB depth ~10 km below sea level), a steady-state initial temperature profile with an LAB depth equal to 50 km is imposed so that $z_{LAB}^0 = 50$ km when magmatism occurs. In practice, this constraint means initially placing the 1175°C isotherm at a depth of 50 km. This assumption is consistent with both the results of our geochemical modeling and tomographically constrained LAB depth beneath intraplate magmatic provinces. Second, we assume that the less conductive oceanic crustal layer is 20 km rather than 7 km thick, a choice that reflects elevated thickness beneath magmatic provinces relative to standard oceanic crust. Note that we ignore the effects of viscoelastic relaxation, which

means that the topographic load generated by this thicker crust is instantaneously compensated. Finally, observational studies have strongly suggested that initial excess subsidence of ocean islands is generated by movement away from swell bathymetry that is at least partly generated by excess mantle temperatures (38). Hence, to account for the excess heat provided by a putative mantle plume, initial steady-state temperature profiles corresponding to elevated initial mantle potential temperature, $(T_p)_0$, are imposed. As the thermal structure evolves, $(T_p)_0$ decays linearly over time (30 Ma) to the ambient mantle value adopted by Richards *et al.* (28), $T_p = 1333°C$ (see Materials and Methods). This evolving temperature excess is initially imposed at the base of the thermal boundary layer (i.e., the shallowest depth at which $\frac{dT}{dz}$ drops below $0.5°C\,km^{-1}$), before deepening at a rate of 10 mm year^{-1}. This progressive temperature decay and vertical advection of the thermal boundary simulate the movement of the plate away from a plume-like mantle heat source (38). We test the effect of varying the decay time of this thermal anomaly and its precise parametrization, but it makes minimal difference to our results (see section S5). To find the optimum plate model that best describes our $z_{LAB}(t)$ observations, we carry out a grid search in which pairs of z_p and $(T_p)_0$ are systematically explored and optimized.

Our results show that cooling and rethickening of the lithosphere from an initial thickness of ~50 km following the cessation of magmatism can explain the distribution of oceanic LAB depth as a function of time since magmatic eruption. The optimal plate thickness is closely comparable to that obtained by fitting global oceanic bathymetry and heat flow data as a function of plate age (23, 28). The significant difference is that while the best-fitting value of z_p is only ~17 ± 10 km in excess of that required to explain global oceanic subsidence and heat flow, an initial excess temperature anomaly of between 0 and +200°C relative to the global background is required to fit $z_{LAB}(t)$ beneath intraplate magmatic provinces [Fig. 3A; (28)]. This temperature anomaly then wanes rapidly. This result is consistent with both excess asthenospheric potential temperatures associated with at least some proportion of intraplate magmatism and constraints from the drowning of ocean islands (20, 38, 39).

Continental LIPs

Next, we extend this model to the continental realm. First, we maintain the condition that the initial LAB depth is 50 km (i.e., $z_{LAB}^0 = 50$ km). This assumption is supported by modeling of REE compositions of mafic and ultramafic melts in LIP magmas (39). Second, we assume that continental crustal thickness, $z_{cc} = 35$ km, and account for differences in thermal properties associated with its more felsic composition including enhanced radiogenic heat production, H^*, and higher thermal conductivity [see Materials and Methods; (42)]. As before, the initial temperature profile is determined by finding the steady-state geotherm, given the value of $(T_p)_0$, that results in the 1175°C isotherm at a depth of 50 km. We carry out a grid search to determine the best-fitting values of $(T_p)_0$ and z_p that are consistent with observed values of z_{LAB} as a function of LIP age. The Deccan Traps are excluded from our analysis since its two contributing temporal bins are clear outliers (see section S5).

Results show that, as for the oceans, the thickness of the lithospheric mantle beneath continental LIPs can be fitted with a simple adapted plate-cooling model, although with some significant differences. The best-fitting potential temperature is $(T_p)_0 = 1465 \pm$

120°C, which, while less well defined, overlaps with the range of values of $(T_p)_0$ in the oceanic realm (Fig. 3). These results suggest that significantly elevated mantle potential temperatures [i.e., $(T_p)_0$ > 1345°C] are a systematic requirement of LIP formation, providing independent evidence for their formation above a mantle plume (39, 43). However, the optimal plate thickness, $z_p = 248$ km, is significantly greater than in the oceans, which implies a steady-state LAB depth of $z_{LAB}^\infty \approx 195$ km. This depth aligns more closely with lithospheric thicknesses inferred from subsidence in intra-cratonic basins (i.e., ~200 km) rather than either subsidence observed in rift basins on non-cratonic continental lithosphere or the ocean floor. [i.e., ~100 to 150 km; (10, 23, 44, 45)]. Note that, although we have chosen to exclude the Deccan Traps outliers from our analysis, the best-fitting value of z_p is minimally affected by their inclusion (i.e., an increase of 1 km), while optimal $(T_p)_0$ remains ~80°C above ambient values (i.e., 1413°C versus 1333°C; see section S5.1).

In summary, our analysis, in which we fit LAB depth estimates with conductive cooling models, suggests that the lithospheric mantle is rapidly thinned immediately before and/or during magmatism in both oceanic and continental realms. It then cools and progressively rethickens following magmatism. For continental LIPs, this thinning is associated with a significant temperature anomaly and steady-state plate thicknesses are similar to those in intra-cratonic basins.

DISCUSSION

Our global analysis of lithospheric thickness beneath intraplate magmatic provinces has shown that magmatism occurs exclusively on thin lithosphere. Following eruption, the lithospheric mantle progressively cools and rethickens to a depth of 125 km in the oceans and 195 km on the continents. These inferences are supported by a range of observations. First, major and trace elemental compositions of recent intraplate magmas suggest that magmatism occurs only where the lithosphere is less than 80 km thick. Second, the thickness of the lithospheric plate calculated by exploiting seismic tomographic models and a calibrated V_S-to-T conversion scheme is in broad agreement with these geochemical estimates. Third, the thickness of the lithosphere beneath ancient intraplate magmatic provinces is systematically thinner than would be expected if they were randomly distributed atop oceanic lithosphere that was following the well-documented plate-cooling relationship. Finally, lithospheric thickness defined by seismic tomographic imaging beneath both oceanic and continental intraplate magmatic provinces systematically increases as a function of eruptive age following a plate cooling relationship subject to initially elevated asthenospheric temperatures. A key observation is that several continental LIPs overlie cratons, which are regions of supposedly ancient, thick, and stable lithospheric mantle (e.g., Karoo, CAMP, Emeishan, Siberia, Kola-Dnieper, Kalkarindji, and Franklin). Our results suggest that even cratonic continental interiors are significantly less stable than often assumed, with cratonic roots apparently neither able to resist being destroyed during LIP emplacement nor remaining permanently thinned after the cessation of magmatism. Here, we discuss the implications of the relationship between LIP emplacement, rapid lithospheric thinning, and protracted thermal relaxation for the compositional makeup of continental lithosphere through time, the formation of economic resources, and the initiation of mass extinction events.
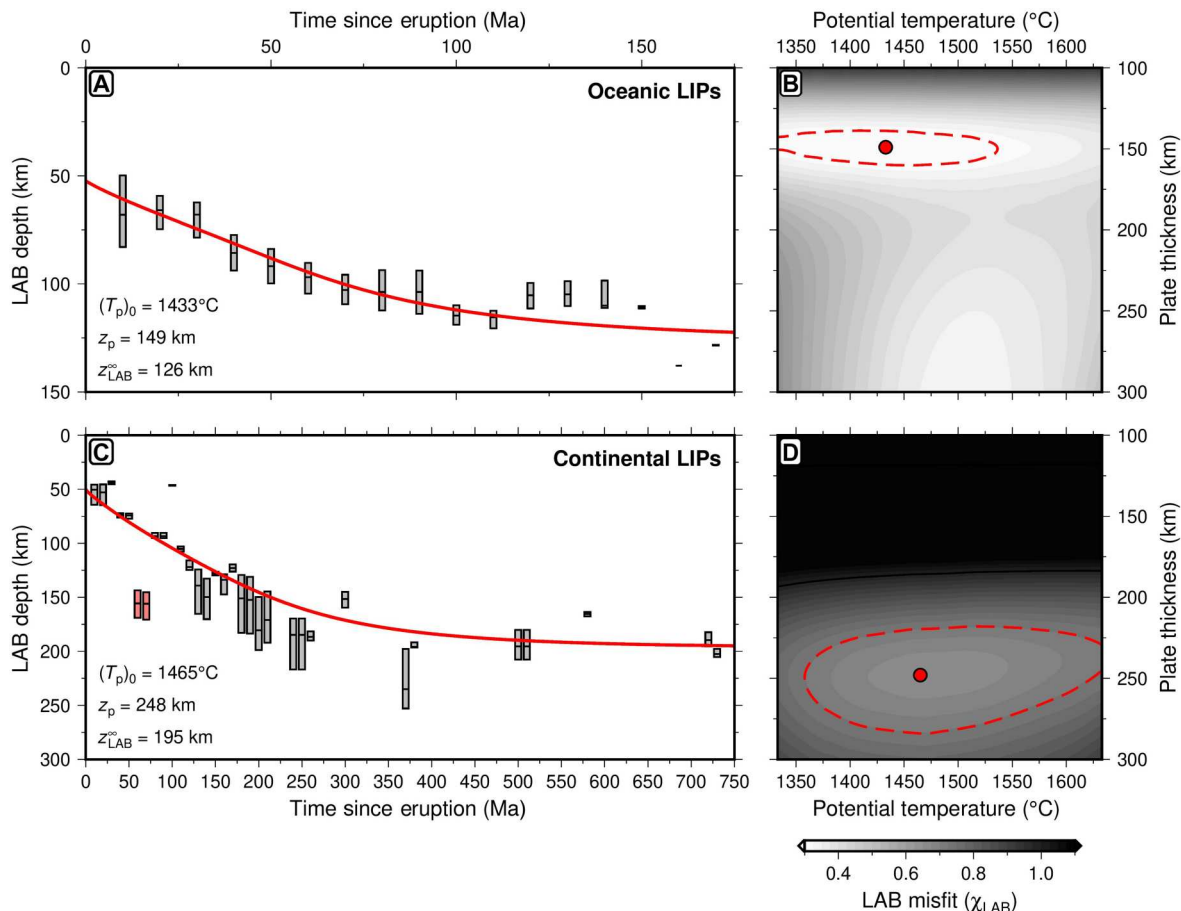
Fig. 3. Lithospheric thermal modeling. (**A**) Observed and modeled LAB depth beneath oceanic intraplate magmatic provinces as a function of time since eruption. Gray bar: interquartile range of LAB depth distribution; red line: best-fitting modeled LAB depth. $(T_p)_0$: initial potential temperature; z_p: plate thickness; z_{LAB}^∞: asymptotic depth to the LAB as $t \to \infty$. (**B**) Misfit between observed and calculated LAB depth as a function of plate thickness, z_p, and initial potential temperature, $(T_p)_0$, for oceanic intraplate magmatism (see Materials and Methods for details). Red circle: misfit minimum; red dashed line: contour marking 1.5× value at misfit minimum. Optimum values given in lower left-hand corner of (A). (**C**) Observed and modeled LAB depth beneath continental LIPs as a function of time since eruption. Red bars: Deccan Traps, excluded from the analysis. (**D**) As (B) but for continental LIPs. Optimum values of $(T_P)_0$, z_p, and z_{LAB}^∞ given in lower left-hand corner of (C).

Recratonization

Previous insights indicate that thick, cratonic lithosphere is likely to have been generated by high degrees of melt extraction at shallow depths followed by lithospheric thickening during ancient (i.e., pre-Phanerozoic) orogenic events [see (15, 46) and references therein]. Our results, however, suggest that in some locations, this preexisting lithospheric mantle is destroyed before, or during, LIP eruption. It is then reemplaced over the subsequent ~300 Ma by thermal relaxation (Figs. 2B and 3C). Compositional differences between unperturbed and rethickened cratonic lithosphere are challenging to distinguish geophysically. However, our results allow useful constraints to be placed upon the compositional evolution of cratonic roots during and after magmatism.

LIPs often appear on ancient cratons (e.g., Siberia, Karoo, Central Atlantic Magmatic Province, and Franklin), which are likely to have depleted, low-density lithospheric roots (16). Thinning of undepleted lithospheric mantle is a significant means of generating topographic uplift and denudation on 10^3 km length scales (47). Conversely, thickening of an undepleted lithospheric root drives time-dependent subsidence (48). Lithospheric depletion

(i.e., density reduction, $\Delta\rho$) modulates the amplitude of this uplift and subsidence. Consider a cratonic setting where the onset of magmatism is associated with a combination of a transient asthenospheric thermal anomaly and removal of an ancient, thermally equilibrated, and depleted (i.e., low-density) cratonic root (Fig. 4, A and B). In this case, the initial density of the root, ρ_m^*, is perhaps 50 kg m^{-3} lower than in non-cratonic lithospheric mantle. Removal of this somewhat depleted root and the subplate thermal anomaly together lead to significant amounts of air-loaded surface uplift [i.e., $U_o = 1.8$ km if $(T_p)_0 = 1465$°C; see Materials and Methods]. Note that if ρ_m^* is significantly more depleted, then the magnitude of this uplift decreases substantially (e.g., $U_o \approx$ 500 m for depletion of 80 kg m^{-3}). Subsequent thermal reequilibration drives regrowth of the lithospheric mantle (Fig. 4, C to G). If this regrowing lithospheric mantle is completely undepleted, then the result is net air-loaded subsidence of 1.6 km after 350 Ma and 2.1 km after 750 Ma. No net uplift or subsidence occurs when rethickening mantle lithosphere is depleted by 50 kg m^{-3} (i.e., same density as precursor lithospheric mantle, ρ_m^*). Finally, if depletion is
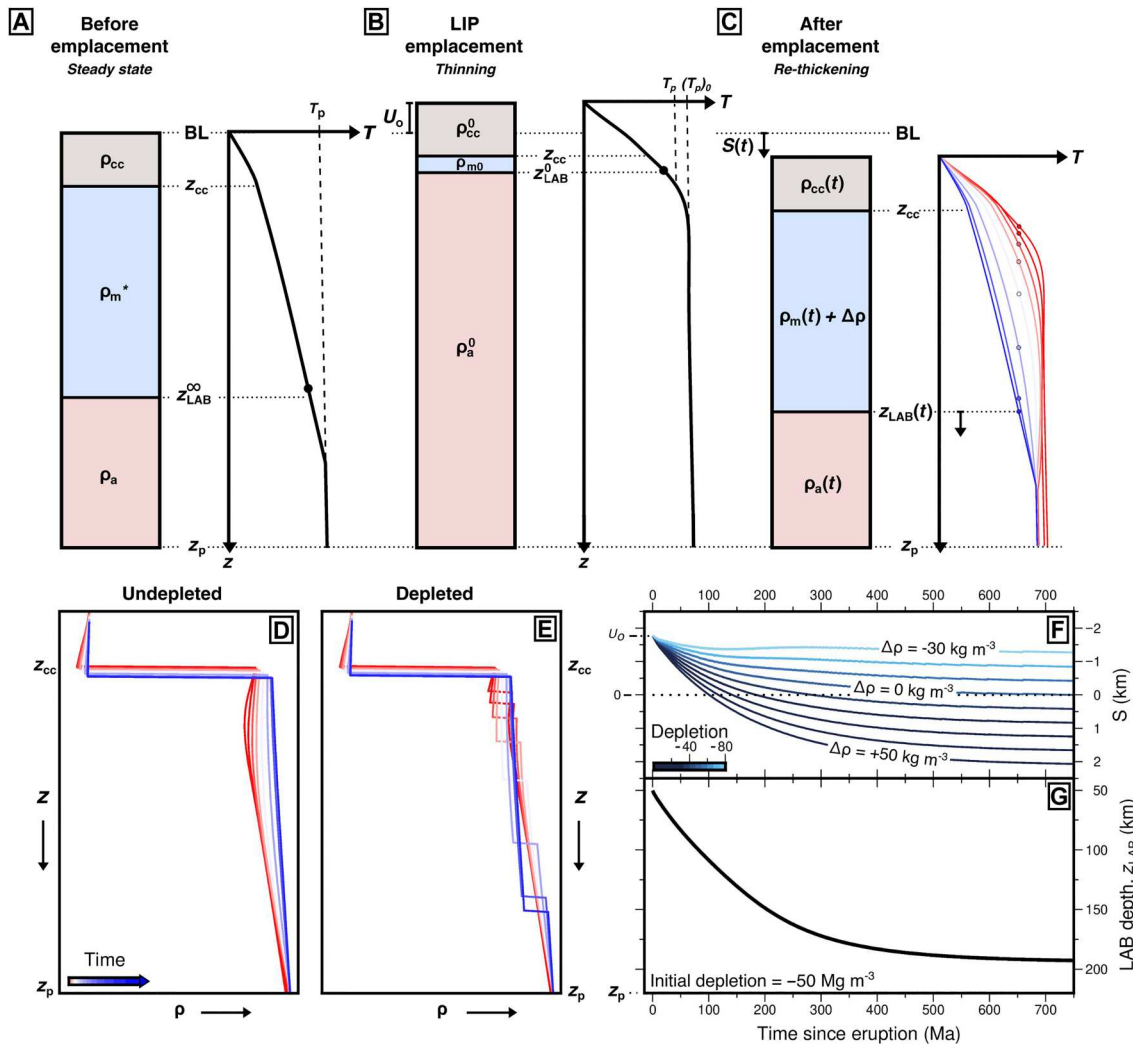
Fig. 4. Thermal, depletion, and subsidence modeling. (**A**) Pair of cartoons showing continental column and temperature profile of precursory lithosphere in thermal steady state before LIP emplacement. z_{LAB}^{∞}: steady-state LAB depth, defined by 1175°C isotherm; z_{cc}: crustal thickness; z_p: plate thickness; ρ_{cc}: steady-state crustal density; ρ_m^*: steady-state initial lithospheric mantle density; ρ_a: steady-state asthenospheric density; T_p: ambient mantle potential temperature; BL: base level (i.e., initial elevation of top of lithospheric column). (**B**) Thinned lithospheric column during LIP emplacement at $t = 0$, where $z_{LAB}^0 = 50$ km; U_o: initial uplift driven by thinning of plate and subplate thermal anomaly; ρ_m^0: lithospheric mantle density; ρ_a^0: asthenospheric mantle density; $(T_p)_0$: elevated mantle potential temperature. (**C**) Subsidence as $z_{LAB}(t)$ deepens from z_{LAB}^0 to z_{LAB}^{∞}. $\rho_{cc}(t)$: crustal density as a function of time; $\rho_m(t)$: lithospheric mantle density as a function of time; $\rho_a(t)$: asthenospheric mantle density as a function of time; $\Delta\rho$: density difference as a result of depletion between precursor, ρ_m^*, and final lithospheric mantle density, ρ_m^{∞}; $S(t)$: time-dependent net subsidence (i.e., above or below base level, $S(\infty) = 0$ km if $\Delta\rho = 0$ Mg m^{-3}. (**D**) Density as a function of depth for undepleted lithospheric mantle colored by time since eruption (i.e., red to blue through time). (**E**) As (D) with depleted lithospheric mantle, $\Delta\rho = -50$ kg m^{-3}. (**F**) Air-loaded subsidence as a function of time since eruption, $S(t)$, for various values of $\Delta\rho$ after thinning precursory lithosphere with initial depletion = -50 kg m^{-3} from $z_{LAB}^{\infty} = 200$ km to $z_{LAB}^0 = 50$ km. Negative values indicate uplift. $U_o = 1.76$ km is transient initial uplift. Note if rethickening lithosphere more depleted than original lithosphere net uplift generated when $t \rightarrow \infty$. Dotted line: no net uplift or subsidence. Labeled lines colored by depletion relative to ambient (undepleted) mantle. Labels: values of $\Delta\rho$. Negative values are density reductions due to increased depletion. (**G**) Depth to LAB as a function of time since eruption, $z_{LAB}(t)$.

increased to 80 kg m^{-3}, then a total of 1.3 km of net uplift is generated after 750 Ma (Fig. 4, F and G; Materials and Methods).

Extensive evidence exists for uplift associated with intraplate magmatism, although in cratonic regions it can be controversial [e.g., (20, 43, 49–51)]. This controversy perhaps indicates the relatively modest magnitude of initial uplift expected as a result of rapid thinning of depleted cratonic lithosphere. This more modest magnitude is in contrast to the kilometer-scale uplift expected to result from removing the same thickness of fertile lithosphere [e.g., (47,

52, 53)]. A second important observation is that many LIPs that overlie reequilibrated lithosphere (i.e., $t_0 > 300$ Ma) are exposed at the surface today and not buried under deep sedimentary basins. It is therefore likely that they have experienced either net uplift or at least no appreciable net vertical motion between the pre-magmatism and post-equilibration lithospheric states. Together with the results of our simple modeling, these observations suggest that depleted cratonic lithosphere is removed before or during magmatism and then it is replaced by similarly or more depleted lithospheric

mantle during subsequent thermal relaxation. LIP emplacement therefore provides a mechanism for cratonic destruction followed by recratonization.

Additional evidence corroborates this conclusion. There are two reasons to expect that the crust may sometimes be thinned during the emplacement of an LIP, which would be expected to generate even further net subsidence after lithospheric reequilibration (i.e., when z_{LAB} reaches z_{LAB}^{∞}). First, the initial asthenospheric thermal pulse and lithospheric removal generate excess topography that is progressively eroded, resulting in crustal thinning (54). Second, many—but not all—LIPs are associated with some amount of lithospheric extension. These processes are offset to some degree by the addition of erupted, intruded, and underplated basaltic material that would tend to thicken the crust (54). It is important to note, however, that all that remains of many LIPs is the plumbing system, the flood basalts having been totally denuded [e.g., (18, 55)]. To expose LIP plumbing systems at the surface rather than have them buried under kilometers of sediment and lava flows, post-LIP topography must acquire permanent subcrustal support. Lithospheric depletion, potentially modulated by magmatic underplating, is a plausible mechanism for this topographic support. An important corollary is that initial uplift, erosion, and replacement of depleted lithospheric mantle with a subsequently less depleted (i.e., denser, in this case) lithospheric keel could be a way to generate subsidence in intra-cratonic basins.

This argument suggests that the emplacement of an LIP is likely responsible for local-to-regional destruction of cratonic lithospheric mantle on short time scales, followed by recratonization on longer time scales. There is a caveat worth highlighting, however. Our analysis provides neither an estimate for the precise thickness and composition of the preexisting lithospheric mantle beneath individual LIPs nor a definitive explanation for the mechanism of lithospheric mantle thinning. For example, it is possible that a mantle plume could be directed by basal lithospheric topography into a preexisting lithospheric thin spot [e.g., (5, 56, 57)]. There, it would generate surface uplift and extensive magmatism due to its excess potential temperature, before growth of a depleted, neutrally buoyant lithospheric root begins after magmatism, resulting in net-neutral topography. This situation may yield a similar suite of observations to those in the previously discussed case, where a neutrally buoyant cratonic root is first removed. However, independent constraints on paleo-lithospheric thickness from both the presence of kimberlites and the reconstruction of geothermal gradients using thermobarometry of mantle xenoliths indicate that the lithosphere was thick before several African magmatic events where it is now thinner [see, e.g., (19, 53, 58)]. Similar observations are also found in the MacKenzie Flood Basalt Province, Canada (21). Furthermore, our results themselves suggest that thin spots are short lived and heal in the absence of perturbation. Basal thermal erosion by a mantle plume has been proposed as a mechanism for thinning the lithospheric mantle, but this process is challenging to achieve on short time scales (58). Alternatively, melt and fluid infiltration could lead to refertilization and subsequent destabilization of the lithospheric keel (15, 59, 60).

Regardless of the precursory state of the mantle, simple geodynamic reasoning further supports rethickening of the lithospheric mantle after magmatism by progressive cooling of depleted restites. The equilibrium thickness of undepleted continental lithospheric mantle is around 100 to 150 km (48). We find that the equilibrium

thickness of the thermal boundary layer in continental regions affected by LIP emplacement is closer to 180 to 220 km. McKenzie and Richter (61) showed that the thickness of the upper thermal boundary layer, δ, is proportional to $v^{\frac{1}{3}}$, where v is kinematic viscosity (i.e., η/ρ, where η is dynamic viscosity and ρ is density). At a given temperature, melt depletion leads to an increase in viscosity of the mantle residue [e.g., (62)]. Hence, a doubling of v leads to an increase in δ of around one quarter. Geochemical depletion of the uppermost mantle therefore leads to a thickening of the upper thermal boundary layer relative to ambient mantle.

Although time-dependent deepening of the LAB is a globally robust relationship, excess deepening is not observed in the oceanic realm, where z_{LAB}^{∞} = 125 km. In the oceans, the LAB seldom exceeds depths of >150 km, regardless of the presence or absence of LIPs. Furthermore, in the oceans, significant post-magmatic subsidence is observed (37, 38). A mechanism is therefore needed to rethicken depleted mantle on the continents while perhaps not in the oceans. Numerical modeling carried out by Liu et al. (21) indicates that lithospheric thin spots surrounded by thick cratonic lithosphere can trap accumulations of low-density, depleted mantle material. This material can be generated by in situ melt extraction within the plume head during LIP formation or can be composed of remnant parcels of previously removed cratonic mantle. Their results show that in these circumstances the lithosphere can recover up to 90% of its original thickness as depleted residue cools over the subsequent 300 Ma, almost entirely healing any putatively destroyed precursory cratonic lithospheric mantle. By contrast, their analysis implies that when LIPs are emplaced in oceanic regions distant from thick cratonic lithosphere, melt-depleted material is more easily entrained into the sublithospheric mantle, limiting the eventual rethickening of the oceanic lithosphere. Our observations strongly support this idea and suggest that, despite their rarity, where plumes are able to erode the cratonic lithospheric mantle, plume-driven recratonization is routine in the continental realm.

Economic resources

Our results provide a predictive framework for modeling the thermal evolution of undeformed continental interiors in response to magmatic events. The thinning and rethickening pattern can act as a useful tool to highlight and evaluate prospects for economic resources that are dependent on the thermal evolution of the lithosphere, including critical minerals [e.g., (8)]. For example, diamonds primarily form within cold, thick continental lithospheric roots (i.e., 1130° ± 120°C at 5.3 ± 0.8 GPa) and are brought to the surface within kimberlite pipes (63). Our results suggest that thinning of the plate during/before emplacement of an LIP will suppress diamond formation and entrainment for ~300 Ma as the plate rethickens beyond ≳170 km (Fig. 2B). Several LIPs are spatially proximal to older, diamondiferous and/or younger, barren kimberlite fields. Such locations include the Siberian Traps, which erupted 75 to 45 Ma after the diamondiferous Alakit, Upper Muna, and Daldyn fields and 0 to 30 Ma before the barren, traps-related Kharamay field (64). The Keweenawan LIP on the southern Superior craton, North America, erupted 1150 to 1100 Ma before present, and preceded/coincided with the barren 1100-Ma-old Kyle Lake kimberlite field. Crucially, however, the much more recent Attawapiskat kimberlites, which occurred in the same location 180 to 150 Ma before present, were diamondiferous (65). Similar logic applies

to the Artemisia kimberlites, which became diamondiferous 600 Ma after emplacement of the MacKenzie Flood Basalts above the Slave Craton, Canada (21). Previous authors have tied these relationships to the heating of lithospheric roots out of the diamond-bearing window by mantle plumes during LIP events (19, 66, 67). We contend that rapid and wholesale lithospheric removal may be a key mechanism (19). Moreover, our observations reveal a predictive time scale over which cratonic keels will return to a state favorable to diamond formation, which is similar to results of previous modeling studies [~300 Ma, (21)].

Climate change and mass extinctions

Finally, our results have implications beyond the solid Earth since LIP eruptions release large quantities of chemical species that can lead to global environmental change. When carbon, sulfur, and halogens are expelled into the atmosphere, they warm the planet, cool the planet, and deplete the ozone layer, respectively (68). The rapid and large-scale eruption of these climate-forcing gases during LIP emplacement is thought to be responsible for many of Earth's mass extinctions [see, e.g., (69) and references therein]. The Siberian Traps ($\sim 1 \times 10^6$ to 2×10^6 km^3) coincides with the largest known extinction event, which defines the Permian-Triassic boundary and represents the loss of >80% of marine species (70). However, conventional mantle plume-derived melts are insufficiently concentrated in C, S, and halogens to generate the catastrophic environmental change required to drive such a mass extinction (3, 68). Metasomatized continental lithospheric mantle, on the other hand, is rich in these elements (71). Analysis of mantle xenoliths emplaced during and after eruption of the Siberian Traps demonstrates that the subcontinental lithospheric mantle stored abundant halogens, ~70% of which were scavenged by ascending melts (71). Therefore, destruction of the subcontinental lithospheric mantle and release of the volatiles it contains during LIP formation is a viable trigger for the Permian-Triassic boundary extinction, and was probably enhanced by release of S and C from sediments as a result of magmatic heating (71–73). While it has been previously argued that destruction of the lithospheric mantle beneath the very largest LIPs contributes to the most significant mass extinction events, a temporal, if not mechanistic, link has also been drawn between mass extinctions and smaller LIPs. For example, the Emeishan Traps, which are around $\sim 3 \times 10^5$ km^3 in volume (i.e., <1/3 Siberian Traps), and erupted above the Yangtze Craton, have been linked to the end-Guadalupian mass extinction event (74). Alteration and removal of the lithospheric mantle beneath even the smaller LIPs could therefore be a contributing factor to the environmental forcing that leads to mass extinction events.

MATERIALS AND METHODS
LIP database

Coffin and Eldholm (35) and Coffin et al. (36) mapped the outlines of Phanerozoic LIPs and oceanic seamounts, and provided approximate eruption ages for each location. We have updated this database to include LIPs up to 750 Ma. We further amended the ages and outlines of a number of polygons contained in the original database to honor updated radiometric dates. A list of sources for the updated database can be found in the Supplementary Materials (datasets S3 and S5).

Seismologic estimates of lithospheric thickness

Throughout this study, we exploit the lithospheric thickness model of Hoggard et al. (8). This model converts shear-wave velocities, V_S, into temperature, T, using the calibration method of Richards et al. (24) and the upper-mantle V_S tomographic model of Schaeffer and Lebedev (75). This temperature conversion scheme relies on the experiment-based parameterization of Yamauchi and Takei (76), which accounts for the effects of anelasticity on V_S as the mantle melting temperature is approached. The equations include seven material constants that are calibrated by exploiting the thermal structure beneath mid-oceanic ridges in four different ways. First, V_S profiles are extracted along oceanic plate flow lines and are averaged to yield V_S as a function of plate age and depth. These stacked profiles are then compared to predicted values of V_S from applying the V_S-to-T conversion to a plate-cooling model (23). Misfit is calculated between observed and modeled V_S at depth slices of 87.5 and 112.5 km. Since oceanic plate thickness is generally ≤125 km, it is not possible to use this approach at greater depths. Second, V_S profiles are averaged globally at depths beneath the thermal boundary layer (i.e., between 225 and 400 km) and are compared to values of V_S predicted by applying the V_S-to-T conversion to a mantle isentrope with a potential temperature, T_p = 1333°C, which is assumed to represent ambient mantle. Third, the globally averaged shear wave attenuation as a function of depth beneath old (>100 Ma) oceanic lithosphere is calculated from V_S using the same conversion and compared to published estimates at depths >150 km. Finally, the misfit between published and calculated depth-averaged mantle viscosity beneath the thermal boundary layer is evaluated.

These four misfit functions are combined, weighted, and minimized to optimize the values of the seven unknown material constants in the anelastic parameterization. Finally, lithospheric thickness is calculated globally by extracting the 1175°C isotherm, which is assumed to be a proxy for the depth to the base of the mechanical boundary layer. For further details on the methodology, see Hoggard et al. (8) and Richards et al. (24).

Geochemical estimates of lithospheric thickness
Major element thermobarometry

Partitioning of major elements between melt and solid mantle is pressure and temperature dependent. The Plank and Forsyth (25) thermobarometer exploits a comprehensive suite of melt equilibration experiments to parameterize the response of major element composition to pressure and temperature changes. To estimate lithospheric thickness, we apply this thermobarometer to a global database of Neogene-Quaternary mafic intraplate magmatic samples compiled by Ball et al. (20). These calculations are carried out using meltPT—an open-source Python library designed for whole-rock thermobarometric analysis [https://github.com/fmcnab/meltPT; (26)].

Before estimating melt equilibration conditions, the effects of fractional crystallization are mitigated by filtering our magmatic database so that all samples have 9 < MgO < 14.5 wt %. Samples must also include a measurement of Ce concentration so that H_2O can be estimated assuming that H_2O/Ce = 200 (77, 78). We calculate the primary melt compositions of each sample by adding olivine that is in equilibrium with the melt until olivine forsterite content is 0.9 (79). Since only Fe^{2+} is compatible within olivine, an estimate of $Fe^{3+}/\Sigma Fe$ is required. We assume that $Fe^{3+}/\Sigma Fe$ = 0.2, which is

halfway between the average values for theoliitic and alkali basalts (80).

These primary melt compositions are used to generate estimates of the pressure and temperature at which mantle melts equilibrated [i.e., P_{eq} and T_{eq}, respectively (25)]. Samples may have last equilibrated within the lithosphere or asthenosphere, and the boundary between these layers is defined throughout our study by the 1175°C isotherm. In a given location, we assume that the maximum lithospheric thickness coincides with the equilibration pressure of the shallowest sample that has an equilibration temperature $T_{eq} >$ 1175°C since temperatures cooler than this value are likely to indicate that equilibration occurred within the lithosphere. To estimate lithospheric thickness globally, we subdivide our thermobarometric results into 1° × 1° geographic bins. We only estimate lithospheric thickness for bins with ≥10 samples since smaller sample sizes are less likely to capture the LAB.

REE inverse modeling
We exploit the results of REE inverse modeling presented by Ball et al. (20), who use an adapted form of the INVMEL-v12 forward model to simulate partitioning of trace elements between melt and residue within the mantle during melting (81). REE concentrations along adiabatic melt paths are calculated, and misfit between observed and synthetic REE concentrations is minimized using a grid search procedure. Ball et al. (20) collect their data into 1° × 1° geographic bins and calculate an optimum melt path for each bin. The upper limit of the melting region is assumed to represent the LAB (20). Note that this definition is slightly different to the isothermal definition used elsewhere in our study. The partitioning of each REE depends upon the bulk source composition, the aluminous phase present in the source, as well pressure and temperature. Ball et al. (20) filter their database for 8.5 < MgO < 14.5 wt % to mitigate fractionation effects, and they use εNd as a proxy for source composition. Finally, they place the garnet-spinel transition zone at 63 to 72 km (82).

Statistical analyses
Weighted median
To mitigate skewness and suppress outliers, we calculate the median when averaging data. For ease of analysis, we have divided Earth's surface into 1° × 1° bins. To avoid oversampling higher latitudes and biasing median values, we weight each lithospheric thickness data point, z_i, by latitude, ϕ_i. To achieve this weighting, we construct a data vector, $\mathbf{z}$, and a weights vector, $\mathbf{w}$, where each weight is given by $\cos\phi_i$. The weighted median is calculated by sorting $\mathbf{z}$ and $\mathbf{w}$ in ascending order by the values of $\mathbf{z}$. The median value is given by z_j, where the index, j, of the sorted data vector is calculated by minimizing

$$j = \min_k \left[\sum_{i=1}^{k} w_i z_i > \frac{1}{2} \sum_{i=1}^{n} w_i z_i \right] \quad (1)$$

For even-length data vectors, we use the upper-weighted median so that z_j is given by $(z_j + z_{j+1})/2$. We calculate the weighted interquartile range of the distribution by changing the prefactor of $\frac{1}{2}$ in Eq. 1 to $\frac{1}{4}$ and $\frac{3}{4}$ for upper and lower quartiles, respectively.

Predicted oceanic lithospheric thickness distribution
Seamounts can only form on oceanic crust that is the same age, or older, than themselves. For example, a suite of seamounts erupting at the present day (i.e., 0 Ma) can cap oceanic crust that formed

between the present day and Jurassic times. The median age of the seafloor beneath these seamounts will therefore lie somewhere between the two and be skewed toward younger ages since there is much more young oceanic crust than old on Earth (Fig. 1A). Moreover, a seamount that is 200 Ma can only be located on crust ≥200 Ma, most of which has been subducted and lost from the surface record. Consequently, since lithospheric plate thickness increases with age, we expect to observe a positive relationship between seamount age and LAB depth.

Richards et al. (23, 24) constructed an oceanic plate-cooling model that simultaneously minimizes the misfit between global databases of heat flow and bathymetric observations that have been corrected for sediment and crustal loading. Their approach includes both pressure- and temperature-dependent thermal properties. We assume that the LAB within this plate-cooling model coincides with the 1175°C isotherm [i.e., consistent with the LAB model of Hoggard et al. (8)]. We predict the unperturbed depth to the modern-day LAB, z_{LAB}^1, by extracting LAB depth as a function of age from this plate model using the oceanic crustal age model of Müller et al. (27), which was updated to include additional data by Richards et al. (23). The predicted value is compared to thickness implied by seismic tomography, which is in close agreement [see Fig. 1C; (8, 75)].

Oceanic crustal ages, t_{crust}, and LAB depths range from 0 Ma to t_{max} and from $z_{LAB}(0)$ to $z_{LAB}(t_{max})$, respectively. Seamounts cannot form on plates younger than their eruption age, t_0, and if $t_0 > t_{max}$, then they would not be recorded on Earth's surface today. Therefore, the thickness of lithosphere on which seamounts are located ranges from $z_{LAB}(t_0)$ to $z_{LAB}(t_{max})$. For each eruption age, we record the lithospheric thickness distribution of oceanic crustal ages where $t_0 < t_{crust} < t_{max}$. The median and interquartile range of predicted lithospheric thickness as a function of t_0 (i.e., the blue line in Fig. 3D) is calculated using Eq. 1.

Lithospheric modeling
Parameterization
To model lithospheric rethickening following periods of active magmatism, we solve the one-dimensional heat equation expressed as

$$\rho(P, T, X) C_P(T, X) \frac{\partial T}{\partial t} = \frac{\partial}{\partial z} \left[k(P, T, X) \frac{\partial T}{\partial z} \right] + H^*(X) \quad (2)$$

where t is the time, z is the depth, T is the temperature, P is the pressure, X is the composition, ρ is the density, C_P is the isobaric specific heat capacity, k is the thermal conductivity, and H^* is the internal radiogenic heat production.

Equation 2 is solved numerically with an unconditionally stable time- and space-centered Crank-Nicholson finite difference scheme and a predictor-corrector step (83). Accordingly, Eq. 2 is recast as

$$T_j^{n+1} + A \left[-\frac{k_{j+\frac{1}{2}}^m}{\Delta z_j^m} T_{j+1}^{n+1} + \left(\frac{k_{j+\frac{1}{2}}^m}{\Delta z_j^m} + \frac{k_{j-\frac{1}{2}}^m}{\Delta z_{j-1}^m} \right) T_j^{n+1} - \frac{k_{j-\frac{1}{2}}^m}{\Delta z_{j-1}^m} T_{j-1}^{n+1} \right]$$
$$= T_j^n + A \left[\frac{k_{j+\frac{1}{2}}^m}{\Delta z_j^m} T_{j+1}^n - \left(\frac{k_{j+\frac{1}{2}}^m}{\Delta z_j^m} + \frac{k_{j-\frac{1}{2}}^m}{\Delta z_{j-1}^m} \right) T_j^n + \frac{k_{j-\frac{1}{2}}^m}{\Delta z_{j-1}^m} T_{j-1}^n \right] + A H_j^{*m} (\Delta z_j^m + \Delta z_{j-1}^m)$$
$$(3)$$

where

$$A = \frac{\Delta t}{[\rho_j^m C_{P j}^m (\Delta z_j^m + \Delta z_{j-1}^m)]} \quad (4)$$

and Δt is the time step, Δz is the depth spacing between nodes, and n and j are the time and depth indices, respectively. Equation 3 is solved by tridiagonal elimination (83). For the initial predictor phase of each time step, $m = n$, while in the subsequent corrector phase, $m = n + \frac{1}{2}$. We use a Lagrangian reference frame, whereby Δz_j^m is initially set to 1 km (i.e., when $m = 0$) and then scales with thermal contraction in subsequent time steps. These time steps are calculated using a Courant-Friedrichs-Lewy condition calculated according to

$$\Delta t = \min_j \left[\frac{(\Delta z_j^0)^2 \rho_j^0 C_{Pj}^0}{2.2 k_j^0} \right] \sim 5 \text{ kyr} \tag{5}$$

T^{n+1} typically converges to within a tolerance of 0.001°C after the corrector phase.

Boundary conditions
All models consist of crustal and mantle layers. Crustal thickness for oceanic and continental regions is set to $z_{oc} = 20$ km and $z_{cc} = 35$ km, respectively. In both cases, the underlying mantle extends from the Moho to an assumed equilibrium plate thickness, z_p. The initial depth to the LAB, after the cessation of magmatic activity and lithospheric thinning, is assumed to be $z_{LAB}^0 = 50$ km. To account for the possible presence of a mantle plume beneath the plate, initial asthenospheric potential temperature, $(T_p)_0$, can vary between 1333°C, which is assumed to be the temperature of ambient mantle, and 1633°C (i.e., an excess temperature of 300°C).

Separate parameterizations are used to define the thermophysical properties of the crust and mantle (k, C_P, ρ, and $H^\star$). Crustal radiative thermal conductivity and ρ are determined using the Richards et al. (28) parameterization, but the reference density, ρ_0, is dependent on whether oceanic or continental lithosphere is to be modeled (2950 and 2700 kg m^{-3}, respectively). In the continental crust, C_P and lattice thermal diffusivity, κ_{lat}, are calculated using the parameterization of Whittington et al. (42), and $H^\star$ is assumed to be 0.7 µW m^{-3} (8). In oceanic crust, we use the Richards et al. (28) parameterization for C_P and κ_{lat}, and assume $H^\star = 0$ mW m^{-3}. In both the continental and oceanic mantle, the temperature- and pressure-dependent formulations specified in Richards et al. (28) are adopted, with radiogenic heat production assumed to be negligible ($H^\star = 0$ µW m^{-3}).

Initial temperature profiles are obtained by combining the parameters outlined above with the equations of McKenzie et al. (84). In all cases, kinematic viscosity, ν, is assumed to be 9×10^{19} m^2 s^{-1}. For each combination of z_{oc} or z_{cc}, and $(T_p)_0$, we find the steady-state geotherm consistent with z_{LAB}^0 by iterating through a range of mechanical boundary layer thicknesses (2 to 60 km). We select the temperature profile with depth to the 1175°C isotherm equal to z_{LAB}^0.

To simulate the waning of a plume-derived heat source through time, we impose an evolving basal boundary condition. At $t = 0$, $T(z)$ is given by the initial isentrope defined by $(T_p)_0$ below the base of the thermal boundary layer (i.e., the shallowest depth at which the geothermal gradient, $\frac{\partial T}{\partial z}$, drops below 0.5°C km^{-1}). In later time steps, the depth at which this boundary condition is imposed, z_b, increases according to a prescribed plume sinking rate, $v_{plume} = 10$ mm year^{-1}, until the deepest model node (i.e., $z_b = z_p$) is reached, whereupon the basal boundary depth remains fixed. Simultaneously, from $t = 0$ to 30 Ma, the temperature

applied at the basal boundary decays linearly to that of the ambient mantle isentrope (i.e., $T_p = 1333$°C) at the relevant depth. Beyond $t = 30$ Ma, the basal temperature is assumed to remain equal to that of the ambient mantle isentrope at the appropriate depth.

Optimization strategy
We carry out a two-parameter sweep to find the combination of plate thickness, z_p, and initial potential temperature, $(T_p)_0$, that best explains our constraints on $z_{LAB}(t)$. For each $[z_p, (T_p)_0]$ pair, we find the initial steady-state thermal structure that yields $z_{LAB}^0 = 50$ km. Note that, if the lithospheric mantle is instantaneously thinned, it is likely that the remaining mantle will not be thermally equilibrated. Nonetheless, since the conductive layer is thin, it will rapidly reach steady state and so the effect of thermal disequilibration is likely to be minor. We then calculate $z_{LAB}(t)$, for $0 < t < t_{max}$ Ma, where $t_{max} = 750$ Ma, using Eq. 3. To minimize the misfit between tomographically determined LAB depth and predicted LAB depth as a function of age beneath LIPs, we use the trial function

$$\chi = \sqrt{\frac{1}{M} \sum_{i=1}^{M} \left(\frac{z_i^o - z_i^c}{\sigma_i} \right)^2} \tag{6}$$

where z_i^o and z_i^c are observed and calculated LAB depth, σ_i is the standard deviation of the ith measurement, and M is the number of estimates. We used weighted binned median lithospheric thickness estimates, where

$$\sigma_i = \frac{\sqrt{(IQR_1^i)^2 + (IQR_2)^2}}{1.349} \tag{7}$$

and IQR_1^i is the interquartile range of the ith measurement and $IQR_2 = 25$ km is the approximate vertical uncertainty of the lithospheric thickness grid. Note that this relationship assumes that errors are normally distributed.

Subsidence
Air-loaded subsidence of the surface for our pressure- and temperature-dependent plate model is given by

$$S(t) = \int_0^{z_p} \left[1 - \frac{\rho(0, z')}{\rho(t, z')} \right] dz' \tag{8}$$

where z' is the Lagrangian depth coordinate that deepens as the column is compressed. Since many ancient LIPs are located above continental shields, we assume that the pre-LIP lithospheric mantle (i.e., where $z_{cc} < z < z_{LAB}$) was in thermal equilibrium, cratonic, and that precursory lithospheric mantle density, ρ_m^*, is depleted by -50 Mg m^{-3} relative to ambient mantle (i.e., 3280 Mg m^{-3} at surface temperature and pressure relative to an ambient value of 3330 Mg m^{-3}; Fig. 4A). The effect of changes in lithospheric depletion following LIP emplacement is explored by adding $\Delta\rho$ (i.e., $\Delta\rho$ is negative for more depleted lithosphere) to all values of $\rho(t, z')$ that are located at depths within the lithospheric mantle. For simplicity, we assume that the steady-state thermal structure of the lithospheric column before thinning and after rethickening are identical and given by the results of our thermal evolution modeling (i.e., z_{LAB}^∞; Fig. 3D). We explore initial geotherms that are out of thermal equilibrium in the Supplementary Materials. Initial uplift, $U_o = S(0)$, after thinning is calculated using Eq. 8; thence, $S(t)$ is calculated

using a range of values of $\Delta\rho$ to explore the effect of lithospheric melt depletion upon subsidence of the Earth's surface (Fig. 4).

Supplementary Materials

This PDF file includes:
Sections S1 to S5
Figs. S1 to S17
Legend for data files S1 to S6
References

Other Supplementary Material for this manuscript includes the following:
Data files S1 to S6

REFERENCES AND NOTES

1. D. McKenzie, M. J. Bickle, The volume and composition of melt generated by extension of the lithosphere. *J. Petrol.* **29**, 625–679 (1988).
2. S. D. King, D. L. Anderson, Edge-driven convection. *Earth Planet. Sci. Lett.* **160**, 289–296 (1998).
3. N. H. Sleep, Survival of Archean cratonal lithosphere. *J. Geophys. Res. Solid Earth* **108**, (2003).
4. A. Lenardic, L.-N. Moresi, H. Mühlhaus, Longevity and stability of cratonic lithosphere: Insights from numerical simulations of coupled mantle convection and continental tectonics. *J. Geophys. Res. Solid Earth* **108**, (2003).
5. D. R. Davies, N. Rawlinson, G. Iaffaldano, I. H. Campbell, Lithospheric controls on magma composition along Earth's longest continental hotspot track. *Nature* **525**, 511–514 (2015).
6. Y. Niu, Lithosphere thickness controls the extent of mantle melting, depth of melt extraction and basalt compositions in all tectonic settings on earth—A review and new perspectives. *Earth Sci. Rev.* **217**, 103614 (2021).
7. P. Molnar, P. England, Late Cenozoic uplift of mountain ranges and global climate change: Chicken or egg? *Nature* **346**, 29–34 (1990).
8. M. J. Hoggard, K. Czarnota, F. D. Richards, D. L. Huston, A. L. Jaques, S. Ghelichkhan, Global distribution of sediment-hosted metals controlled by craton edge stability. *Nat. Geosci.* **13**, 504–510 (2020).
9. M. Hoggard, J. Austermann, C. Randel, S. Stephenson, Observational estimates of dynamic topography through space and time, in *Mantle Convection and Surface Expressions* (American Geophysical Union, 2021), pp. 371–411.
10. B. Parsons, J. G. Sclater, An analysis of the variation of ocean floor bathymetry and heat flow with age. *J. Geophys. Res.* **82**, 803–827 (1977).
11. J. Jackson, D. McKenzie, K. Priestley, B. Emmerson, New views on the structure and rheology of the lithosphere. *J. Geol. Soc.* **165**, 453–465 (2008).
12. W. L. Griffin, S. Y. O'Reilly, J. C. Afonso, G. C. Begg, The composition and evolution of lithospheric mantle: A re-evaluation and its tectonic implications. *J. Petrol.* **50**, 1185–1204 (2009).
13. M. E. Pasyanos, T. G. Masters, G. Laske, Z. Ma, LITHO1.0: An updated crust and lithospheric model of the Earth. *J. Geophys. Res. Solid Earth* **119**, 2153–2173 (2014).
14. J. C. Afonso, N. Rawlinson, Y. Yang, D. L. Schutt, A. G. Jones, J. Fullea, W. L. Griffin, 3-D multiobservable probabilistic inversion for the compositional and thermal structure of the lithosphere and upper mantle: III. Thermochemical tomography in the Western-Central U.S. *J. Geophys. Res. Solid Earth* **121**, 7337–7370 (2016).
15. D. G. Pearson, J. M. Scott, J. Liu, A. Schaeffer, L. H. Wang, J. van Hunen, K. Szilas, T. Chacko, P. B. Kelemen, Deep continental roots and cratons. *Nature* **596**, 199–210 (2021).
16. T. H. Jordan, Composition and development of the continental tectosphere. *Nature* **274**, 544–548 (1978).
17. C. J. O'Neill, A. Lenardic, W. L. Griffin, S. Y. O'Reilly, Dynamics of cratons in an evolving mantle. *Lithos* **102**, 12–24 (2008).
18. R. E. Ernst, A. Dickson, A. Bekker, in *Large Igneous Provinces: A Driver of Global Environmental and Biotic Changes*, R. E. Ernst, A. J. Dickson, A. Becker, eds. (American Geophysical Union, 2021), vol. 255 of *Geophysical Monograph Series*, pp. 3–26.
19. N. L. Celli, S. Lebedev, A. J. Schaeffer, M. Ravenna, C. Gaina, The upper mantle beneath the South Atlantic Ocean, South America and Africa from waveform tomography with massive data sets. *Geophys. J. Int.* **221**, 178–204 (2020).
20. P. W. Ball, N. J. White, J. Maclennan, S. N. Stephenson, Global influence of mantle temperature and plate thickness on intraplate volcanism. *Nat. Commun.* **12**, 2045 (2021).
21. J. Liu, D. G. Pearson, L. H. Wang, K. A. Mather, B. A. Kjarsgaard, A. J. Schaeffer, G. J. Irvine, M. G. Kopylova, J. P. Armstrong, Plume-driven recratonization of deep continental lithospheric mantle. *Nature* **592**, 732–736 (2021).
22. C. J. Grose, J. C. Afonso, Comprehensive plate models for the thermal evolution of oceanic lithosphere. *Geochem. Geophys. Geosyst.* **14**, 3751–3778 (2013).
23. F. D. Richards, M. J. Hoggard, L. Cowton, N. J. White, Reassessing the Thermal Structure of Oceanic Lithosphere With Revised Global Inventories of Basement Depths and Heat Flow Measurements. *J. Geophys. Res. Solid Earth* **123**, 9136–9161 (2018).
24. F. D. Richards, M. J. Hoggard, N. White, S. Ghelichkhan, Quantifying the relationship between short-wavelength dynamic topography and thermomechanical structure of the upper mantle using calibrated parameterization of anelasticity. *J. Geophys. Res. Solid Earth*, e2019JB019062 (2020).
25. T. Plank, D. Forsyth, Thermal structure and melting conditions in the mantle beneath the Basin and Range province from seismology and petrology. *Geochem. Geophys. Geosyst.* **17**, 1312–1338 (2016).
26. F. McNab, P. W. Ball, meltPT: A Python package for basaltic whole-rock thermobarometric analysis with application to Hawai'i. *Volcanica* **6**, 63–76 (2023).
27. R. D. Müller, N. Flament, K. J. Matthews, S. E. Williams, M. Gurnis, Formation of Australian continental margin highlands driven by plate–mantle interaction. *Earth Planet. Sci. Lett.* **441**, 60–70 (2016).
28. F. Richards, M. Hoggard, A. Crosby, S. Ghelichkhan, N. J. White, Structure and dynamics of the oceanic lithosphere-asthenosphere system. *Phys. Earth Planet. In.* **309**, 106559 (2020b).
29. F. A. Darbyshire, I. T. Bjarnason, R. S. White, Ó. G. Flóvenz, Crustal structure above the iceland mantle plume imaged by the icemelt refraction profile. *Geophys. J. Int.* **135**, 1131–1149 (1998).
30. J. Jenkins, J. Maclennan, R. G. Green, S. Cottaar, A. F. Deuss, R. S. White, Crustal formation on a spreading ridge above a mantle plume: Receiver function imaging of the icelandic crust. *J. Geophys. Res. Solid Earth* **123**, 5190–5208 (2018).
31. B. M. Le, T. Yang, J. P. Morgan, Seismic constraints on crustal and uppermost mantle structure beneath the hawaiian swell: Implications for plume-lithosphere interactions. *J. Geophys. Res. Solid Earth*, e2021JB023822 **127**, (2022).
32. N. Schmerr, The gutenberg discontinuity: Melt at the lithosphere-asthenosphere boundary. *Science* **335**, 1480–1483 (2012).
33. I. Guest, G. Ito, M. O. Garcia, E. Hellebrand, Extensive magmatic heating of the lithosphere beneath the Hawaiian Islands inferred from salt lake crater mantle xenoliths. *Geochem. Geophys. Geosyst.* **21**, e2020GC009359 (2020).
34. A. Pleus, G. Ito, P. Wessel, L. N. Frazer, Rheology and thermal structure of the lithosphere beneath the Hawaiian ridge inferred from gravity data and models of plate flexure. *Geophys. J. Int.* **222**, 207–224 (2020).
35. M. F. Coffin, O. Eldholm, Large igneous provinces: Crustal structure, dimensions, and external consequences. *Rev. Geophys.* **32**, 1 (1994).
36. M. F. Coffin, R. A. Duncan, O. Eldholm, J. G. Fitton, F. A. Frey, H. C. Larsen, J. J. Mahoney, A. D. Saunders, R. Schlich, P. J. Wallace, Large igneous provinces and scientific ocean drilling: Status quo and a look ahead. *Oceanography* **19**, 150–160 (2006).
37. R. S. Detrick, S. T. Crough, Island subsidence, hot spots, and lithospheric thinning. *J. Geophys. Res. Solid Earth* **83**, 1236 (1978).
38. K. L. Huppert, J. T. Perron, L. H. Royden, Hotspot swells and the lifespan of volcanic ocean islands. *Sci. Adv.* **6**, eaaw6906 (2020).
39. R. S. White, D. McKenzie, Mantle plumes and flood basalts. *J. Geophys. Res. Solid Earth* **100**, 17543–17585 (1995).
40. T. H. Torsvik, M. A. Smethurst, K. Burke, B. Steinberger, Large igneous provinces generated from the margins of the large low-velocity provinces in the deep mantle. *Geophys. J. Int.* **167**, 1447–1460 (2006).
41. C. A. Stein, S. Stein, Constraints on hydrothermal heat flux through the oceanic lithosphere from global heat flow. *J. Geophys. Res. Solid Earth* **99**, 3081–3095 (1994).
42. A. G. Whittington, A. M. Hofmeister, P. I. Nabelek, Temperature-dependent thermal diffusivity of the earth's crust and implications for magmatism. *Nature* **458**, 319–321 (2009).
43. A. D. Saunders, S. M. Jones, L. A. Morgan, K. L. Pierce, M. Widdowson, Y. G. Xu, Regional uplift associated with continental large igneous provinces: The roles of mantle plumes and the lithosphere. *Chem. Geol.* **241**, 282–318 (2007).
44. R. Newman, N. White, The dynamics of extensional sedimentary basins: Constraints from subsidence inversion. *Philos. Trans. R. Soc. A* **357**, 805–834 (1999).
45. J. J. Armitage, P. A. Allen, Cratonic basins and the long-term subsidence history of continental interiors. *J. Geol. Soc.* **167**, 61–70 (2010).
46. C.-T. A. Lee, P. Luffi, E. J. Chin, Building and destroying continental mantle. *Annu. Rev. Earth Planet. Sci.* **39**, 59–90 (2011).

47. P. Bird, Continental delamination and the colorado plateau. *J. Geophys. Res. Solid Earth* **84**, 7561–7571 (1979).

48. D. McKenzie, Some remarks on the development of sedimentary basins. *Earth Planet. Sci. Lett.* **40**, 25–32 (1978).

49. B. He, Y.-G. Xu, S.-L. Chung, L. Xiao, Y. Wang, Sedimentary evidence for a rapid, kilometer-scale crustal doming prior to the eruption of the emeishan flood basalts. *Earth Planet. Sci. Lett.* **213**, 391–405 (2003).

50. X. Wang, L. Shao, K. A. Eriksson, Z. Yan, J. Wang, H. Li, R. Zhou, J. Lu, Evolution of a plume-influenced source-to-sink system: An example from the coupled central emeishan large igneous province and adjacent western yangtze cratonic basin in the late permian, sw china. *Earth Sci. Rev.* **207**, 103224 (2020).

51. S. N. Stephenson, N. J. White, A. Carter, D. Seward, P. W. Ball, M. Klöcking, Cenozoic dynamic topography of Madagascar. *Geochem. Geophys. Geosyst.* **22**, e2020GC009624 (2021).

52. A. Sembroni, C. Faccenna, T. W. Becker, P. Molin, B. Abebe, Long-term, deep-mantle support of the Ethiopia-Yemen plateau. *Tectonics* **35**, 469–488 (2016).

53. M. Klöcking, M. J. Hoggard, V. Rodríguez Tribaldos, F. D. Richards, A. R. Guimarães, J. Maclennan, N. J. White, A tale of two domes: Neogene to recent volcanism and dynamic uplift of northeast Brazil and southwest Africa. *Earth Planet. Sci. Lett.* **547**, 116464 (2020).

54. J. Brodie, N. White, Sedimentary basin inversion caused by igneous underplating: Northwest european continental shelf. *Geology* **22**, 147–150 (1994).

55. K. L. Buchan, R. E. Ernst, A giant circumferential dyke swarm associated with the high arctic large igneous province (halip). *Gondw. Res.* **58**, 39–57 (2018).

56. J. De Laat, S. Lebedev, N. L. Celli, R. Bonadio, B. C. de Melo, N. Rawlinson, Structure and evolution of the Australian plate and underlying upper mantle from waveform tomography with massive data sets. *Geophys. J. Int.* **234**, 153–189 (2023).

57. A. Boscaini, A. Marzoli, H. Bertrand, M. Chiaradia, F. Jourdan, M. Faccenda, C. M. Meyzen, S. Callegaro, L. Serrano Durán, Cratonic keels controlled the emplacement of the central atlantic magmatic province (camp). *Earth Planet. Sci. Lett.* **584**, 117480 (2022).

58. K. A. Mather, D. G. Pearson, D. McKenzie, B. A. Kjarsgaard, K. Priestley, Constraints on the depth and thermal history of cratonic lithosphere from peridotite xenoliths, xenocrysts and seismology. *Lithos* **125**, 729–742 (2011).

59. S. F. Foley, Rejuvenation and erosion of the cratonic lithosphere. *Nat. Geosci.* **1**, 503–510 (2008).

60. J. Hu, L. Liu, M. Faccenda, Q. Zhou, K. M. Fischer, S. Marshak, C. Lundstrom, Modification of the western gondwana craton by plume–lithosphere interaction. *Nat. Geosci.* **11**, 203–210 (2018).

61. D. McKenzie, F. M. Richter, Parameterized thermal convection in a layered region and the thermal history of the earth. *J. Geophys. Res. Solid Earth* **86**, 11667 (1981).

62. A. H. Peslier, A. B. Woodland, D. R. Bell, M. Lazarov, Olivine water contents in the continental lithosphere and the longevity of cratons. *Nature* **467**, 78–81 (2010).

63. T. Stachel, R. W. Luth, Diamond formation—Where, when and how? *Lithos* **220-223**, 200–220 (2015).

64. J. Sun, C. Z. Liu, S. Tappe, S. I. Kostrovitsky, F. Y. Wu, D. Yakovlev, Y. H. Yang, J. H. Yang, Repeated kimberlite magmatism beneath Yakutia and its relationship to Siberian flood volcanism: Insights from in situ U–Pb and Sr–Nd perovskite isotope analysis. *Earth Planet. Sci. Lett.* **404**, 283–295 (2014).

65. K. V. Smit, T. Stachel, R. A. Stern, Diamonds in the Attawapiskat area of the Superior craton (Canada): Evidence for a major diamond-forming event younger than 1.1 Ga. *Contrib. Mineral. Petrol.* **167**, 962 (2014).

66. H. Helmstaedt, J. Gurney, Geotectonic controls of primary diamond deposits: Implications for area selection. *J. Geochem. Explor.* **53**, 125–144 (1995).

67. R. E. Ernst, D. R. Davies, S. M. Jowitt, I. H. Campbell, When do mantle plumes destroy diamonds? *Earth Planet. Sci. Lett.* **502**, 244–252 (2018).

68. H. Sigurdsson, Evidence of volcanic loading of the atmosphere and climate response. *Global Planet. Change* **3**, 277–289 (1990).

69. B. A. Black, L. T. Elkins-Tanton, M. C. Rowe, I. U. Peate, Magnitude and consequences of volatile release from the Siberian Traps. *Earth Planet. Sci. Lett.* **317**, 363 (2012).

70. S. M. Stanley, Estimates of the magnitudes of major marine mass extinctions in earth history. *Proc. Natl. Acad. Sci. U.S.A.* **113**, E6325–E6334 (2016).

71. M. W. Broadley, P. H. Barry, C. J. Ballentine, L. A. Taylor, R. Burgess, End-Permian extinction amplified by plume-induced release of recycled lithospheric volatiles. *Nat. Geosci.* **11**, 682–687 (2018).

72. C. Ganino, N. T. Arndt, Climate changes caused by degassing of sediments during the emplacement of large igneous provinces. *Geology* **37**, 323–326 (2009).

73. J. Guex, S. Pilet, O. Müntener, A. Bartolini, J. Spangenberg, B. Schoene, B. Sell, U. Schaltegger, Thermal erosion of cratonic lithosphere as a potential trigger for mass-extinction. *Sci. Rep.* **6**, 23168 (2016).

74. M.-F. Zhou, J. Malpas, X. Y. Song, P. T. Robinson, M. Sun, A. K. Kennedy, C. M. Lesher, R. R. Keays, A temporal link between the Emeishan large igneous province (SW China) and the end-Guadalupian mass extinction. *Earth Planet. Sci. Lett.* **196**, 113–122 (2002).

75. A. J. Schaeffer, S. Lebedev, Global shear speed structure of the upper mantle and transition zone. *Geophys. J. Int.* **194**, 417–449 (2013).

76. H. Yamauchi, Y. Takei, Polycrystal anelasticity at near-solidus temperatures. *J. Geophys. Res. Solid Earth* **121**, 7790–7820 (2016).

77. J. E. Dixon, L. Leist, C. Langmuir, J.-G. Schilling, Recycled dehydrated lithosphere observed in plume-influenced mid-ocean-ridge basalt. *Nature* **420**, 385–389 (2002).

78. F. McNab, P. W. Ball, M. J. Hoggard, N. J. White, Neogene uplift and magmatism of Anatolia: Insights from drainage analysis and basaltic geochemistry. *Geochem. Geophys. Geosyst.* **19**, 175–213 (2018).

79. C. T. A. Lee, P. Luffi, T. Plank, H. Dalton, W. P. Leeman, Constraints on the depths and temperatures of basaltic magma generation on Earth and other terrestrial planets using new thermobarometers for mafic magmas. *Earth Planet. Sci. Lett.* **279**, 20–33 (2009).

80. D. Canil, R. D. Hyndman, D. Fode, Hygrometric control on the lithosphere-asthenosphere boundary: A 28 million year record from the Canadian Cordillera. *Geophys. Res. Lett.* **48**, e2020GL091957 (2021).

81. D. McKenzie, R. K. O'Nions, Partial melt distributions from inversion of rare earth element concentrations. *J. Petrol.* **32**, 1021–1091 (1991).

82. E. S. Jennings, T. J. B. Holland, A simple thermodynamic model for melting of peridotite in the system NCFMASOCr. *J. Petrol.* **56**, 869–892 (2015).

83. W. H. Press, S. A. Teukolsky, W. T. Vetterling, B. P. Flannery, *Numerical Recipes 3rd Edition: The Art of Scientific Computing* (Cambridge Univ. Press, 2007).

84. D. McKenzie, J. Jackson, K. Priestley, Thermal structure of oceanic and continental lithosphere. *Earth Planet. Sci. Lett.* **233**, 337–349 (2005).

85. M. J. Hoggard, J. Winterbourne, K. Czarnota, N. White, Oceanic residual depth measurements, the plate cooling model and global dynamic topography. *J. Geophys. Res. Solid Earth* **122**, 2328–2372 (2017).

86. J. G. Negi, O. P. Pandey, P. K. Agrawal, Super-mobility of hot indian lithosphere. *Tectonophysics* **131**, 147–156 (1986).

87. J. Sharma, M. R. Kumar, K. S. Roy, P. N. S. Roy, Seismic imprints of plume-lithosphere interaction beneath the Northwestern Deccan Volcanic Province. *J. Geophys. Res. Solid Earth* **123**, 10,831–10,853 (2018).

88. P. K. Patro, S. V. S. Sarma, Lithospheric electrical imaging of the deccan trap covered region of western India. *J. Geophys. Res. Solid Earth* **114**, (2009).

89. C. Ebinger, T. Bechtel, D. Forsyth, C. Bowin, Effective elastic plate thickness beneath the East African and Afar plateaus and dynamic compensation of the uplifts. *J. Geophys. Res. Solid Earth* **94**, 2883–2901 (1989).

90. J. Weber, The structures of the Alpha Ridge, Arctic Ocean and Iceland-Faeroe Ridge, North Atlantic: Comparisons and implications for the evolution of the Canada Basin. *Mar. Geol.* **93**, 43–68 (1990).

91. A. Døssing, H. R. Jackson, J. Matzka, I. Einarsson, T. M. Rasmussen, A. V. Olesen, J. M. Brozena, On the origin of the Amerasia Basin and the High Arctic Large Igneous Province—Results of new aeromagnetic data. *Earth Planet. Sci. Lett.* **363**, 219–230 (2013).

92. F. Riefstahl, S. Estrada, W. H. Geissler, W. Jokat, R. Stein, H. Kämpf, P. Dulski, R. Naumann, C. Spiegel, Provenance and characteristics of rocks from the Yermak Plateau, Arctic Ocean: Petrographic, geochemical and geochronological constraints. *Mar. Geol.* **343**, 125–145 (2013).

93. R. A. Duncan, Age progressive volcanism in the new england seamounts and the opening of the central atlantic ocean. *J. Geophys. Res. Solid Earth* **89**, 9980–9990 (1984).

94. R. V. Santos, C. E. Ganade, C. M. Lacasse, I. S. L. Costa, I. Pessanha, E. P. Frazão, E. L. Dantas, J. A. Cavalcante, Dating Gondwanan continental crust at the Rio Grande Rise, South Atlantic. *Terra Nova* **31**, 424–429 (2019).

95. S. Homrighausen, K. Hoernle, F. Hauff, J. A. Wartho, P. van den Bogaard, D. Garbe-Schönberg, New age and geochemical data from the Walvis Ridge: The temporal and spatial diversity of South Atlantic intraplate volcanism and its possible origin. *Geochim. Cosmochim. Acta* **245**, 16–34 (2019).

96. T. M. Maia, A. C. dos Santos, E. R. V. Rocha-Júnior, C., M. de, Valeriano, J. C. Mendes, I. K. Jeck, W. H. dos Santos, A. L. de Oliveira, W. U. Mohriak, First petrologic data for vitória seamount, vitória-trindade ridge, south atlantic: A contribution to the trindade mantle plume evolution. *J. South Am. Earth Sci.* **109**, 103304 (2021).

97. K. Sreejith, K. Krishna, Magma production rate along the Ninetyeast Ridge and its relationship to Indian plate motion and Kerguelen hot spot activity. *Geophys. Res. Lett.* **42**, 1105–1112 (2015).

98. E. Bredow, B. Steinberger, Variable melt production rate of the Kerguelen hotspot due to long-term plume-ridge interaction. *Geophys. Res. Lett.* **45**, 126–136 (2018).

99. S. Homrighausen, K. Hoernle, J.-A. Wartho, F. Hauff, R. Werner, Do the 85°E Ridge and Conrad Rise form a hotspot track crossing the Indian Ocean? *Lithos* **398-399**, 106234 (2021).

100. A. A. P. Koppers, H. Staudigel, J. R. Wijbrans, M. S. Pringle, The Magellan seamount trail: Implications for Cretaceous hotspot volcanism and absolute Pacific plate motion. *Earth Planet. Sci. Lett.* **163**, 53–68 (1998).

101. A. A. P. Koppers, H. Staudigel, M. S. Pringle, J. R. Wijbrans, Short-lived and discontinuous intraplate volcanism in the South Pacific: Hot spots or extensional volcanism? *Geochem. Geophys. Geosyst.* **4**, (2003).

102. V. Clouard, A. Bonneville, P.-Y. Gillot, The tarava seamounts: A newly characterized hotspot chain on the south pacific superswell. *Earth Planet. Sci. Lett.* **207**, 117–130 (2003).

103. R. A. Duncan, R. A. Keller, Radiometric ages for basement rocks from the Emperor Seamounts, ODP Leg 197. *Geochem. Geophys. Geosyst.* **5**, (2004).

104. V. Clouard, A. Bonneville, Ages of seamounts, islands, and plateaus on the Pacific plate. *Special Pap. Geol. Soc. Am.* **388**, 71 (2005).

105. W. D. Sharp, D. A. Clague, 50-Ma initiation of Hawaiian-Emperor bend records major change in Pacific plate motion. *Science* **313**, 1281–1284 (2006).

106. A. A. P. Koppers, H. Staudigel, J. P. Morgan, R. A. Duncan, Nonlinear ^{40}Ar/^{39}Ar age systematics along the Gilbert Ridge and Tokelau Seamount Trail and the timing of the Hawaii-Emperor Bend. *Geochem. Geophys. Geosyst.* **8**, (2007).

107. C. Adam, A. Bonneville, No thinning of the lithosphere beneath northern part of the Cook-Austral volcanic chains. *J. Geophys. Res. Solid Earth* **113**, (2008).

108. J. Miyata, H. Takayanagi, A. Ishigaki, N. Hirano, S. Shiokawa, A. Nishimura, T. Nakazawa, T. Ishikawa, K. Nagaishi, H. Tokuyama, A. Ishiwatari, Y. Iryu, Tectonic implications of carbonate deposits on the eastern slope of the Hahajima Seamount in the collision zone between the Izu-Bonin Arc and the Philippine Sea Plate and the Ogasawara Plateau on the Pacific Plate. *Island Arc* **29**, e12368 (2020).

109. N. Hirano, H. Sumino, T. Morishita, S. Machida, T. Kawano, K. Yasukawa, T. Hirata, Y. Kato, T. Ishii, A Paleogene magmatic overprint on Cretaceous seamounts of the western Pacific. *Island Arc* **30**, e12386 (2021).

110. R. Pockalny, G. Barth, B. Eakins, K. A. Kelley, C. Wertman, Multiple melt source origin of the Line Islands (Pacific Ocean). *Geology* **49**, 1358–1362 (2021).

111. C. Cordier, H. Delavault, C. Chauvel, Geochemistry of the Society and Pitcairn-Gambier mantle plumes: What they share and do not share. *Geochim. Cosmochim. Acta* **306**, 362–384 (2021).

112. K. Hoernle, A. Schwindrofska, R. Werner, P. van den Bogaard, F. Hauff, G. Uenzelmann-Neben, D. Garbe-Schönberg, Tectonic dissection and displacement of parts of Shona hotspot volcano 3500 km along the Agulhas-Falkland Fracture Zone. *Geology* **44**, 263–266 (2016).

113. N. Parsiegla, K. Gohl, G. Uenzelmann-Neben, The Agulhas Plateau: Structure and evolution of a large igneous province. *Geophys. J. Int.* **174**, 336–350 (2008).

114. S. E. Bryan, L. Ferrari, Large igneous provinces and silicic large igneous provinces: Progress in our understanding over the last 25 years. *GSA Bull.* **125**, 1053–1078 (2013).

115. N. Youbi, R. E. Ernst, U. Söderlund, M. A. Boumehdi, A. A. Lahna, C. C. G. Tassinari, W. El Moume, M. K. Bensalah, The Central Iapetus magmatic province: An updated review and link with the ca. 580 Ma Gaskiers glaciation, in *Geological Society of America Special Paper 544: Mass Extinctions, Volcanism, and Impacts: New Developments*, T. Adatte, D. Bond, G. Kelle, eds. (Geological Society of America, 2020).

116. A. Vorontsov, V. Yarmolyuk, S. Dril, R. Ernst, O. Perfilova, O. Grinev, T. Komaritsyna, Magmatism of the Devonian Altai-Sayan Rift System: Geological and geochemical evidence for diverse plume-lithosphere interactions. *Gondw. Res.* **89**, 193–219 (2021).

117. A. J. Schaeffer, S. Lebedev, Imaging the North American continent using waveform inversion of global and USArray data. *Earth Planet. Sci. Lett.* **402**, 26–41 (2014).

118. N. L. Celli, S. Lebedev, A. J. Schaeffer, C. Gaina, African cratonic lithosphere carved by mantle plumes. *Nat. Commun.* **11**, 92 (2020).

119. E. Debayle, F. Dubuffet, S. Durand, An automatically updated S-wave model of the upper mantle and the depth extent of azimuthal anisotropy. *Geophys. Res. Lett.* **43**, 674–682 (2016).

120. K. Priestley, D. McKenzie, T. Ho, A lithosphere–asthenosphere boundary—A global model derived from multimode surface-wave tomography and petrology, in *Lithospheric Discontinuities*, H. Yuan, B. Romanowicz, eds. (John Wiley and Sons, 2018), chap. 6, pp. 111–124.

121. T. Ho, K. Priestley, E. Debayle, A global horizontal shear velocity model of the upper mantle from multimode love wave measurements. *Geophys. J. Int.* **207**, 542–561 (2016).

122. I. M. Artemieva, Global 1 × 1 thermal model tc1 for the continental lithosphere: Implications for lithosphere secular evolution. *Tectonophysics* **416**, 245–277 (2006).

123. X. Liu, N. Qiu, N. Søager, X. Fu, R. Liu, Geochemistry of late permian basalts from boreholes in the sichuan basin, sw China: Implications for an extension of the emeishan large igneous province. *Chem. Geol.* **588**, 120636 (2022).

124. H. Zhou, K. Hoernle, J. Geldmacher, F. Hauff, D. Garbe-Schönberg, S. Jung, I. Bindeman, Enriched mantle one (emi) type carbonatitic volcanism in namibia: Evidence for a concentrically-zoned Etendeka plume head. *Gondw. Res.* **109**, 239–252 (2022).

125. J. P. Pu, F. A. Macdonald, M. D. Schmitz, R. H. Rainbird, W. Bleeker, B. A. Peak, R. M. Flowers, P. F. Hoffman, M. Rioux, M. A. Hamilton, Emplacement of the Franklin large igneous province and initiation of the Sturtian Snowball Earth. *Sci. Adv.* **8**, eadc9430 (2022).

126. M. I. Kuzmin, V. V. Yarmolyuk, V. A. Kravchinsky, Phanerozoic hot spot traces and paleogeographic reconstructions of the siberian continent based on interaction with the African large low shear velocity province. *Earth Sci. Rev.* **102**, 29–59 (2010).

127. O. P. Polyansky, A. V. Prokopiev, O. V. Koroleva, M. D. Tomshin, V. V. Reverdatto, A. Y. Selyatitsky, A. V. Travin, D. A. Vasiliev, Temporal correlation between dyke swarms and crustal extension in the middle Palaeozoic Vilyui rift basin, Siberian platform. *Lithos* **282-283**, 45–64 (2017).

128. V. Puchkov, R. E. Ernst, M. A. Hamilton, U. Söderlund, N. Sergeeva, A Devonian >2000-km-long dolerite dyke swarm-belt and associated basalts along the Urals-Novozemelian fold-belt: Part of an East-European (Baltica) LIP tracing the Tuzo Superswell. *GFF* **138**, 6–16 (2016).

129. D. A. McConnell, M. J. Goydas, G. N. Smith, J. P. Chitwood, Morphology of the frontal fault zone, southwest oklahoma: Implications for deformation and deposition in the wichita uplift and anadarko basin. *Geology* **18**, 634 (1990).

130. L. Shumlyanskyy, A. Nosova, K. Billström, U. Söderlund, P. G. Andréasson, O. Kuzmenkova, The U–Pb zircon and baddeleyite ages of the Neoproterozoic Volyn Large Igneous Province: Implication for the age of the magmatism and the nature of a crustal contaminant. *GFF* **138**, 17–30 (2016).

131. R. S. White, Mantle plume origin for the karoo and ventersdorp flood basalts, south africa. *South Afr. J. Geol.* **100**, 271–282 (1997).

132. M. A. Coble, G. A. Mahood, Initial impingement of the yellowstone plume located by widespread silicic volcanism contemporaneous with columbia river flood basalts. *Geology* **40**, 655–658 (2012).

133. Y.-G. Xu, X. Wei, Z.-Y. Luo, H.-Q. Liu, J. Cao, The early permian tarim large igneous province: Main characteristics and a plume incubation model. *Lithos* **204**, 20–35 (2014).

Science Advances

Destruction and regrowth of lithospheric mantle beneath large igneous provinces

Simon N. Stephenson, Patrick W. Ball, and Fred D. Richards

View the article online
https://www.science.org/doi/10.1126/sciadv.adf6216
Permissions
https://www.science.org/help/reprints-and-permissions

Use of this article is subject to the Terms of service